Scale-independent relationship between permeability and resistivity in mated fractures with natural rough surfaces

K. Sawayama[1], T. Ishibashi[2], F. Jiang[3,4,5], T. Tsuji[4,6,7], O. Nishizawa[4] , and Y. Fujimitsu[6]

[1]Department of Earth Resources Engineering, Graduate School of Engineering, Kyushu University, Fukuoka, Japan

[2]Fukushima Renewable Energy Institute, National Institute of Advanced Industrial Science and Technology, Koriyama, Japan

[3]Department of Mechanical Engineering, Graduate School of Sciences and Technology for Innovation, Yamaguchi University, Ube, Japan

[4]International Institute for Carbon-Neutral Energy Research, Kyushu University, Fukuoka, Japan

[5]Blue Energy Center for SGE Technology (BEST), Yamaguchi University, Ube, Japan

[6]Department of Earth Resources Engineering, Faculty of Engineering, Kyushu University, Fukuoka, Japan

[7]Disaster Prevention Research Institute, Kyoto University, Uji, Japan

Corresponding author: Kazuki Sawayama (k.sawayama0926@mine.kyushu-u.ac.jp)

Highlights

- Numerical flow simulations reproduce experimental transport properties in fractures
- Fracture permeability and formation factor are scale-independent versus aperture
- Formulates a scale-independent relation between permeability and formation factor
- Empirical parameters of this relation correspond to microstructures of the fracture
- Connectivity of flow paths subdivides the permeability–formation factor relation

Abstract

Geothermal systems consisting of fractures in impermeable rocks are difficult to characterize by in situ methods. In an effort to link characteristics of small-scale and large-scale fractures, this study investigated possible relations between their geophysical parameters. We upscaled the relationship between fracture permeability and formation factor in a laboratory specimen to larger fracture dimensions. Microscopic flow characteristics indicate that this relationship is related to the tortuosity of flow paths. We derived an empirical formula that directly predicts changes in fracture permeability from changes in formation factor. This relation may make it possible to monitor subsurface hydraulic activities through resistivity observations.

Keywords: permeability–formation factor relation, resistivity, fracture permeability, tortuosity, lattice Boltzmann method, enhanced geothermal system

1. Introduction

High-enthalpy geothermal systems generally consist of fracture systems developed in impermeable host rocks (e.g., volcanic rocks, hard pyroclastic rocks, and plutonic rocks). Because fractures in an impermeable rock mass effectively control the bulk flow of a system (Kranz et al., 1979), the behavior of fluid flow in fractures and its temporal changes need to be closely examined and well characterized for sustainable development of geothermal resources. Hydrothermal systems are typically imaged and monitored by geophysical methods such as seismic, electric, and electromagnetic observations. For example, magnetotelluric observations have made it feasible to image hydrothermal systems (Hata et al., 2015; Maithya and Fujimitsu, 2019; Mogi and Nakama, 1993; Tsukamoto et al., 2018) and to detect changes in electrical resistivity associated with hydrothermal activity or hydraulic stimulation of enhanced geothermal systems (EGS) (Abdelfettah et al., 2018; Aizawa et al., 2011; Didana et al., 2017; Jackson et al., 1985; Peacock et al., 2012, 2013). Geothermal developments would benefit if changes in hydraulic properties could be linked to geophysical properties that can be remotely monitored; thus,

investigating these geophysical properties of fractures should lead to better understanding of geothermal systems.

The electric current or fluid flow in fractures can be modeled by a small aperture between parallel plates. Assuming that only an electrolyte in a single fracture carries electric current, the associated electric current I can be described by the linear relation (e.g., Brown, 1989)

$$I = -\frac{W d_e}{\rho} \nabla V, \quad (1)$$

where W is the fracture width, d_e is the electric aperture, ρ is the resistivity, and ∇V is the potential gradient. In contrast, the fluid flow in a fracture is commonly described by the cubic law (e.g., Witherspoon et al., 1980)

$$Q = -\frac{W {d_h}^3}{12\mu} \nabla P, \quad (2)$$

where Q is the flow rate, d_h is the hydraulic aperture, μ is viscosity, and ∇P is the pressure gradient. Because both electrical and hydraulic properties vary with aperture changes, changes in electrical properties could be correlated with changes in hydraulic properties. Electrical properties of rocks often have a linear relationship with permeability in logarithmic coordinates (Archie, 1942; Walsh and Brace, 1984). The electrical conductivity in saw-cut fractures also has a linear relationship with permeability in logarithmic coordinates (Stesky, 1986). In contrast, studies based on single synthetic rough-walled fractures have reported that resistivity and permeability have a nonlinear relationship in logarithmic coordinates (Brown, 1989; Kirkby et al., 2016). This nonlinearity has also been confirmed in numerical simulations of digitized natural rock fractures (Sawayama et al., 2020). The cause of this discrepancy may be the heterogeneous distribution of fracture apertures (or asperities) due to the roughness of fracture surfaces, which causes hydraulic properties to deviate from predictions based on the parallel-plate model, especially under high normal stress (Jager et al., 2007; Pyrak-Nolte et al., 1988; Raven and Gale, 1985; Tsang and Witherspoon, 1981). Because high-enthalpy geothermal systems generally include subsurface fracture systems at depths of 1 km or greater, it is necessary to investigate the hydraulic and electrical properties of rough-walled fractures subjected to high normal stress. Moreover,

74 subsurface stress perturbations induce aperture changes of subsurface fractures, and hence changes in
75 these relationships with aperture closure also need to be understood to monitor transient changes in
76 subsurface hydraulic properties.

77 The heterogeneous distribution of apertures influences the formation of preferential flow paths
78 within fractures, known as the channeling flow (Brown et al., 1998; Ishibashi et al., 2015; Tsang and
79 Tsang, 1987; Vogler et al., 2018; Watanabe et al., 2008). Channeling flow has also been revealed
80 through field observations (Ishibashi et al., 2015; Tsang and Neretnieks, 1998). In geothermal systems,
81 the channeling flow controls the heat-exchange performance of the hot rock mass and the fluid–rock
82 chemical interactions of dissolution and precipitation (Hawkins et al., 2018; Neuville et al., 2010;
83 Okoroafor and Horne, 2019; Sausse, 2002; Singurindy and Berkowitz, 2005). Thus, in addition to
84 fracture permeability, changes in the channeling flow with changes in fracture aperture need to be
85 clarified for a better understanding of hydraulic activities in geothermal systems.

86 Another important issue in interpreting results from field observations is validation of scaling laws
87 between fracture length scales and geophysical properties, because the scaling effect appears in the
88 distribution of apertures in natural rock fractures (Brown, 1995; Brown and Scholz, 1985; Schultz et al.,
89 2008). The aperture structure can be modeled as the contact of two surfaces (footwall and hanging wall)
90 with random surface heights (Brown, 1995). In examinations of the power spectrum density (PSD) of
91 modeled apertures by means of Fourier transforms, the log-log relationship between PSD and aperture
92 wavelengths shows a fractal characteristic at short wavelengths whereby the PSD increases linearly with
93 increasing spatial wavelength, whereas the PSD of the aperture remains constant at wavelengths longer
94 than a particular threshold wavelength because the two surfaces are mated at larger wavelengths. The
95 degree of matedness gradually increases with increasing aperture wavelength (Brown et al., 1986;
96 Glover et al., 1997, 1998a; Ogilvie et al., 2006; Olsson and Brown, 1993). For interpreting field
97 observations, it is thus essential to clarify how this long-wavelength matedness affects the hydraulic and
98 electrical transports. Some studies based on fluid flow experiments and field investigations have
99 suggested that fracture permeability of mated fractures (joints) is scale-dependent (Raven and Gale,

1985; Witherspoon et al., 1979), whereas more recent studies based on experiments and numerical simulations of synthetic fractures (Ishibashi et al., 2015; Matsuki et al., 2006) have concluded that it is scale-independent. Because no study has yet clarified a scaling law of fracture resistivity and the relationship between resistivity and permeability, the application of laboratory-scale results to larger fractures in natural settings requires that the scaling effect be validated by changing length scales of fractures that are mated at longer wavelengths.

In this study, we conducted a laboratory experiment and numerical simulations to investigate the relationship between hydraulic and electrical properties. We first made laboratory observations of the simultaneous changes in fracture permeability and resistivity in a natural fracture in a geothermal rock sample under increasing normal stresses. The experimental data were used for the validation of our digital fracture simulation. In simulations of synthetic fractures of increasing scale, we then explored the scaling effect on fracture permeability, flow area, electrical resistivity, and their respective relationships. The simulations integrated the lattice Boltzmann method for the fluid flow within fractures and the finite-element method for the resistivity calculation (Sawayama et al., 2020). We also evaluated the local behavior of the fluid flow and electric current within fractures to investigate their differences and associated changes in the tortuosity of both flow paths. Our simulations revealed transport behavior, including the 3D flow channels in models of realistic rough-walled fractures, that mimics the hydraulic flow in field fractures. From our results, we propose a scale-independent empirical formula that can predict the changes in fracture permeability directly from the changes in formation factor (the ratio of saturated rock resistivity to fluid resistivity), by which geothermal reservoirs can be better monitored from field geophysical observations.

2. Method

2.1 Laboratory observations

Our initial laboratory experiment measured permeability and electrical resistivity under confining pressures in a rock sample of pyroxene andesite from a fractured core retrieved at a geothermal area in

126 southern Kyushu, Japan. The rock contained a single natural fracture and a matrix consisting of fine-
127 grained quartz, plagioclase, calcite, and chlorite (Sawayama et al., 2018b). The bulk and matrix
128 porosities of the sample were 2.5% and 0.9%, respectively, at atmospheric pressure, as determined by a
129 pycnometer and the difference between the sample's dry and water-saturated mass.

130 The sample was prepared as a cylindrical specimen (35 mm in diameter and 70 mm long) with its
131 flat end surfaces ground parallel to within 0.01 mm, in which the fracture plane was parallel to the central
132 axis. Before the experiment, we used a 3D-measuring microscope (Keyence, VR-3050) to map the
133 topography of the separated fracture walls with a grid of cells 23.433 μm square. We obtained an initial
134 aperture distribution by numerically pairing the fracture surfaces such that they contacted at single points
135 (Fig. 1). The mapped surfaces of the footwall and hanging wall are displayed in Fig. 2. The fracture
136 surfaces mostly mated with a small aperture, except where a few debris particles might represent
137 contamination during sample preparation. These areas were excluded from the spectral analysis of the
138 surface roughness by restricting the analysis to the area within the red outline in Fig. 1. From the PSD
139 slopes of the surface height of the footwall and hanging wall, the fractal dimension *D* was determined
140 as 2.4 (Figure A1 in Appendix A). The threshold wavelength that separates mismatched and mated
141 wavelengths, the mismatch length scale λ_c, was determined as 0.57 mm from the ratio of the PSDs of
142 the fracture surface height and initial aperture (Glover et al., 1998b; Matsuki et al., 2006). Surface
143 roughness σ, defined as the standard deviation of the surface height, was 0.49 mm. These three
144 parameters—the fractal dimension, mismatch length scale, and surface roughness—are generally
145 consistent with previous studies of various types of rock fractures (Table A1 in Appendix A). These
146 parameters were used to generate synthetic fracture models in our numerical simulations.

147 After mapping the fracture surfaces, the specimen was restored to its original state. The fluid flow
148 experiment was then performed under a range of eight confining pressures, P_c, between 6 and 20 MPa.
149 The inlet and outlet pore pressures, P_{in} and P_{out}, were 5 and 4 MPa, respectively. Under each effective
150 normal stress condition ($P_c - (P_{in} + P_{out})/2$), we calculated the fracture permeability k based on

$$k = \frac{{d_h}^2}{12}, \quad (3)$$

where d_h is the hydraulic aperture, estimated by Eq. (2) from the observed flow rates by assuming Darcy flow and neglecting the matrix permeability of the sample, which was less than 10^{-20} m^2.

At each value of normal stress, the electrical impedance was measured along the fluid flow direction employing a four-electrode method and an impedance meter (Solartron Analytical, SI 1260A). The current and voltage electrodes, made of narrow silver net ribbon with AgCl baked coating, were wound around the cylindrical surface of the rock sample. Impedance measurements were performed at a constant AC voltage of 30 mV. We obtained resistivity changes under the eight stress conditions by impedance measurements at the frequency of 10 mHz with the sample's geometric factor (21 mm in length between electrodes and 960 mm^2 in cross-sectional area). The fluid medium was saturated brine (1 wt.% KCl, 1.75 S/m), which had a conductance high enough that surface conduction of the rock matrix could be neglected. Details of the experimental setup were described in Sawayama et al. (2018a).

2.2 Upscaled synthetic fracture model

To apply the results of laboratory-scale investigations to field-scale predictions, the scaling effect in rock properties and their relationships must be clarified. For this purpose, we modeled synthetic fractures with isotropic surfaces that incorporated the fractal characteristics of real rock fracture surfaces and the scaling law of surface roughness (Matsuki et al., 2006). We used the values of fractal dimension D, roughness σ, and mismatch length scale λ_c determined on our natural rock fracture. We first generated a pair of correlated fractal surfaces by inverse Fourier transform of the Fourier components based on fractional Brownian motion (Brown, 1995).

The Fourier components of the footwall $a_{f,xy}$ are a function of the spatial frequency $f = \sqrt{(x^2 + y^2)/L^2}$ in an arbitrary direction according to

$$a_{f,xy} \propto (x^2 + y^2)^{-\frac{4-D}{2}} \exp(2\pi i R_1), \quad (4)$$

where x and y are the node numbers in the x- and y-direction, respectively, and R_1 is a series of uniform random numbers ($0 < R_1 < 1$). Similarly, the Fourier components of the hanging wall $a_{h,xy}$ are

$$a_{h,xy} \propto (x^2 + y^2)^{-\frac{4-D}{2}} \exp\big(2\pi i(R_1 + \gamma(f)R_2)\big), \quad (5)$$

where $\gamma(f)$ expresses the frequency-dependent matedness between the two surfaces and R_2 is a series of uniform random numbers that is independent of R_1. This relation can reproduce a self-similar fracture surface that has the same amplitude as the footwall and a different relative phase, providing a matedness at larger wavelengths and a mismatch at smaller wavelengths. The function $\gamma(f)$ (Matsuki et al., 2006) is equal to 1 (i.e., each surface is totally mismatched) at frequencies at or above the mismatch cutoff frequency f_c (the inverse of λ_c) and takes a value between 0 and 1 (i.e., each surface is partially mated) at frequencies lower than f_c to satisfy

$$2\left(1 - \frac{\sin 2\pi\gamma(f)}{2\pi\gamma(f)}\right) = R(f), \quad (6)$$

where $R(f)$ is the ratio of the PSDs of the linear profiles between the initial aperture and the surface height of the fracture surface. We determined the function $\gamma(f)$ by solving Eq. (6) with the Newton-Raphson method, using $R(f)$ calculated from the profiles of our natural rock fracture (Appendix A):

$$R(f) = \exp(-0.021 \cdot \ln(f)^3 - 0.59 \cdot \ln(f)^2 + 0.72 \cdot \ln(f) - 2.9).$$

As reconstructing the surface roughness of a fracture from the observed spectra is a stochastic process, we needed to examine stochastic fluctuations in models created by different random seeds. We used five different random seeds to validate the repeatability of our simulation results.

After taking the inverse Fourier transform of each Fourier component ($a_{f,xy}$ and $a_{h,xy}$), the surface height is adjusted with an arbitrary proportional constant so that the surface roughness σ satisfies the scaling law

$$\sigma = \sigma_0 \left(\frac{L}{L_0}\right)^{3-D}, \quad (7)$$

where σ_0 is the standard deviation of the surface height along a linear profile of length L_0 on a fracture surface and σ is the standard deviation of the surface height of an arbitrary fracture of length scale L.

In this study, we used L_0 = 24 mm and σ_0 = 0.49 mm from our results for a natural rock fracture (Fig. 1) and generated four different fracture length scales (L = 24 mm, 48 mm, 96 mm, 144 mm). After preparing the digital footwall and hanging wall, we created digital fracture models by numerically pairing the fracture walls with different values of aperture closure.

2.3 Digital fracture simulation

We prepared 3D digital fracture models with a grid size of 0.1 mm, based on the surface topography of the natural fracture walls (Fig. 1), for a series of numerical simulations. The aperture between the two fracture surfaces was adjusted so that the model had a simulated permeability equivalent to that measured in the real fracture (Ishibashi et al., 2015; Sawayama et al., 2020; Watanabe et al., 2008). After the validation of our numerical approach with experimental results, we performed hydraulic and electrical simulations with a series of upscaled synthetic fractures. Using fracture models at four different fracture length scales, we prepared different wall separations ~~with five different random seeds~~ by uniformly reducing the local apertures. The overlapping areas of the fracture surfaces were assumed to be contacting asperities without considering deformation, because the effect of deformation on transport properties is small (Brown, 1989; Ishibashi et al., 2015; Matsuki et al., 2006). The resulting models can mimic both elastic and permanent deformations of contacting asperities to some extent (Brown, 1987; Nemoto et al., 2009; Power and Durham, 1997; Watanabe et al., 2008). Although the voxel size potentially affects the absolute values of hydraulic and electrical properties, we confirmed that results with 0.1 mm and 0.05 mm voxels are similar in our models (Appendix B). We thus concluded that a 0.1 mm voxel system is sufficiently fine for the present study.

Our numerical approach combined lattice Boltzmann fluid flow simulation and finite-element analysis of electrical properties. In lattice Boltzmann modeling, the fluid is modeled by a group of particles, and local fluid flow can be simulated as streaming and collision of these particles. It has a remarkable ability to simulate three-dimensional local flow with complex boundaries, i.e.,

heterogeneous fracture surfaces (He and Luo, 1997; Jiang et al., 2014). This study employed a multi-relaxation-time D3Q19 model (Ahrenholz et al., 2008), of which the governing equation is

$$\boldsymbol{g_i}(\boldsymbol{x} + \boldsymbol{e_i}\,\Delta t,\, t + \Delta t) = \boldsymbol{g_i}(\boldsymbol{x},\, t) + \boldsymbol{\Omega_i}, \quad i = 0, \cdots 18, \tag{8}$$

where Δt is the time step and $\boldsymbol{g_i}(\boldsymbol{x}, t)$ is the particle distribution function that represents the probability of finding a particle at node $\boldsymbol{x}$ and time t with velocity $\boldsymbol{e}_i$. Collision operators $\boldsymbol{\Omega}$ are defined based on equilibrium moments and relaxation rates (Jiang et al., 2014). Three-dimensional water flow is driven by a constant body force from the inlet boundary into the outlet boundary (Fig. 2). Bounce-back boundaries (no-slip scheme at the fluid-solid interfaces) are implemented at the fracture surface, and a periodic boundary is applied along the fracture plane. Lattice Boltzmann simulations enabled us to explore the changes of both microscopic and macroscopic flow with aperture closure. We evaluated the channeling flow using flow area, defined as the ratio of the area of preferential flow paths to the area of the fracture plane (Sawayama et al., 2020; Watanabe et al., 2009), and fracture permeability from the macroscopic flow rate based on Eqs. (2) and (3).

Subsequently, we evaluated the resistivity and the local field of electric currents through the finite-element modeling (Andrä et al., 2013; Garboczi, 1998; Saxena and Mavko, 2016). The local field of electric currents was simulated from the potential difference between the inlet and outlet boundaries in the direction parallel to the fracture plane (and fluid flow direction). In this analysis, fluid and solid, respectively, were modeled with conductivities of 1.75 S/m and 10^{-4} S/m based on the experiment in this study and previous experiments on the same formation under dry conditions (Sawayama et al., 2019). From the electric current field, we then calculated the resistivity associated with an applied voltage parallel to the fluid flow direction based on Ohm's law. We evaluated the bulk resistivity of the specimen with a constant number of grid cells in the z-direction (n_z) to take the resistivity of the matrix rock into account. This evaluation confirmed that n_z does not have a significant effect on the bulk resistivity ρ_b because the rock resistivity is much greater than the fracture resistivity. We then calculated the formation factor F by dividing the bulk resistivity by the fluid resistivity ρ_w, ($F =$

243 ρ_b /ρ_w) so that both effects of the temperature and salinity on fluid resistivity can be neglected. We
244 compared values of *F* for models with different fracture length scales.
245
246 **3. Results**
247 **3.1 Validation with experiments and numerical simulations**
248 Figure 3 shows the experimental and numerical determinations of changes in fracture permeability
249 and resistivity with increasing effective normal stress. For both fracture permeability and resistivity with
250 elevated stress, the experimental and the numerical results show similar trends and fit well with each
251 other. Since our digital fracture simulations reproduce experimental results, the fracture size can be
252 extended to approach a fracture scale in a natural setting. To examine the scaling effect on permeability
253 and resistivity, we upscaled fracture sizes by using synthetic fractures modeled on the natural rock
254 fracture.
255
256 **3.2 Upscaled digital fracture simulations**
257 We conducted a series of digital fracture simulations based on synthetic fracture models having four
258 different fracture length scales (24 mm, 48 mm, 96 mm, and 144 mm) and five different random seeds
259 (Appendix C). Figure 4 shows representative simulation results for flow rates through fractures of
260 different length scales. In models with larger mean aperture (Figs. 4a, d, g, j), the network of dominant
261 flow paths covers most of the area with open spaces (non-zero aperture), indicating that contacting
262 asperities (zero aperture points) trigger the formation of the channeling flow. As the fracture closes,
263 larger fractions of its surfaces are in contact, and hence the dominant flow paths decrease in number.
264 Moreover, non-zero apertures with stagnant flow also form, and these increase in number as contacting
265 asperities surround them (Figs. 4b, e, h, k). When the fracture significantly closes, the flow paths appear
266 to be disconnected (Figs. 4c, f, i, l). Although the number of flow paths and the flow length both increase
267 as the fracture is upscaled, their flow paths within the same unit area (40 mm^2), shown as red outlines
268 in Fig. 4, have similar appearances.

The dominant paths of the electric current are similarly displayed in Fig. 5. As in the case of fluid flow, preferential path networks form that decrease in number with aperture closure. The scale-independent appearance in 40 mm^2 unit areas can also be seen. Electric currents appear to be more diffuse over the fracture than the fluid flow, and this difference becomes significant at maximum aperture closure (Figs. 5c, f, i, l).

Figure 6a shows the vectors of hydraulic flow (in blue) and electrical flow (in red) overlaid at the same position so that the distributions of their respective paths can be compared. These two-dimensional vectors represent summations of the vectors in all cross sections in the z-direction (normal to the fracture plane) and are displayed on the aperture structure (in grayscale). Although hydraulic flow and electric current mostly pass through areas of non-zero aperture, the electric current has a larger number of paths than the hydraulic flow. This indicates that hydraulic flow is affected more strongly than electric current by contacting asperities. The differing sensitivities of hydraulic and electric processes to changes in aperture are the cause of their discrepant streamlines. According to Eqs. (1) and (2), the electric current is linearly dependent on the aperture and the flow rate is proportional to the cube of the aperture. However, cross sections of flow rate (Fig. 6b) and electric current (Fig. 6c) along line X–X′ in Fig. 6a show that our model, in some places, produces smaller fluxes in a larger aperture and larger fluxes in a smaller aperture. This result implies that local apertures are not the sole control of local hydraulic and electrical transport processes in rough-walled fractures. We infer that the connectivity of the path network also has a significant effect on local transport phenomena, as discussed in section 4.1. This is a characteristic that does not appear in the local parallel-plate model of electrical conductance and local flow rate as calculated by Eqs. (1) and (2), respectively.

3.3 Fracture permeability, formation factor, and flow area

The three panels of Fig. 7 show the changes of fracture permeability, formation factor, and flow categories as functions of fracture mean aperture. The three flow categories are the flow area (grid cells occupied by fluid flow as in Fig. 4), the conductive area (cells occupied by electric current as in Fig. 5),

295 and the stagnant area (the rest of the non-contact area in a fracture); the summation of the flow and
296 stagnant areas is not 100% because contacting asperities are also present. These plots indicate no
297 significant differences resulting from the changes of random seeds and scale length, demonstrating both
298 the repeatability of the simulations and the scale-independent characteristics of transport behavior in our
299 simulated fractures. Stochastic fluctuations are small, as we confirmed by using 100 different random
300 seeds (Appendix D).

301 Fracture permeability has a nonlinear relationship with the mean aperture (Fig. 7a). At smaller
302 apertures, permeability deviates from proportionality to the square of the aperture in a parallel-plate
303 model toward smaller values, starting around a mean aperture of 0.15 mm. This result implies that the
304 parallel-plate model overestimates permeability at small apertures because it ignores the roughness
305 effect (Ishibashi et al., 2015; Thompson and Brown, 1991; Zimmerman et al., 1991). The formation
306 factor also has a nonlinear relationship with the mean aperture, increasing as the mean aperture decreases
307 (Fig. 7b). Its rate of increase is smaller than the rate of decrease of fracture permeability, reflecting the
308 different sensitivities of hydraulic and electrical flow to the mean aperture.

309 The flow area decreases with aperture closure as the stagnant area increases correspondingly (Fig.
310 7c). This result demonstrates that regions of streaming and stagnant flow develop at all fracture length
311 scales. The stagnant area reaches a peak when the aperture is small, reflecting the disconnection of flow
312 paths (see Figs. 4c, f, i, l). The conductive area is slightly greater than the flow area at a given aperture,
313 and the gap between them increases with aperture closure. This indicates that the electrical flow is not
314 as strongly affected by the growth of the stagnant area as contacting asperities increase; thus, electrical
315 flow is less strongly dependent on the local aperture.

316

317 **4. Discussion**

318 **4.1 Local transport behavior**

319 Our study found that both hydraulic and electrical flows become highly channelized with the growth
320 of contacting asperities (Figs. 4, 5). These flow paths become fewer with aperture closure as the contact

area and isolated apertures increase. It is notable that electric current paths are more evenly distributed in the fracture than the fluid flow paths, as discussed in section 3.2 (Fig. 6a). Accordingly, the area of electric current is larger than the area of hydraulic flow (Fig. 7c). This discrepancy arises from the different sensitivity of the electrical and hydraulic flows to aperture, the first as a linear function in Eq. (1) and the second as a cubic function in Eq. (2) (Brown, 1989). Whereas flow rate decreases more strongly with aperture closure and local flow directions show more deviations from the global flow direction (i.e., high tortuosity), local current directions deviate less from the global flow direction because the electric current is less sensitive to the aperture (Fig. 6a).

To evaluate the degree of these path deviations, we calculated a weighted average of the local tortuosity τ^2 from the local flow directions (Gueguen and Palciauskas, 1994):

$$\tau^2 = \left(\frac{\delta L'}{\delta L}\right)^2 = \frac{1}{\cos^2\theta}, \quad (9)$$

where δL and $\delta L'$ are the actual path length and apparent path length along the global flow direction, respectively, and the path angle θ is the deviation of the local flow vector from the global flow direction (y-direction); $\theta = 90 \pm 0.1°$ is neglected to eliminate the local error. We calculated the path angle in all grid cells (0.1 mm square), and the overall tortuosity was defined as the average path angle as weighted by the local flow rate or electric current. Figure 8 shows the changes in tortuosity with respect to the mean aperture. The tortuosities of hydraulic and electrical flow paths (hydraulic tortuosity and electric tortuosity hereafter) indicate that hydraulic and electrical flow have different winding characteristics; hydraulic tortuosity is always higher than electrical tortuosity at mean apertures greater than 0.1 mm. The figure also indicates that both tortuosities are scale-independent with respect to the mean aperture.

We validated the results of hydraulic and electrical tortuosities by comparing the simulated results of fracture permeability and formation factor. Considering the equivalent channel model of the parallel-plate (Paterson, 1983; Walsh and Brace, 1984), permeability k and the formation factor F can be rendered as functions of the tortuosity:

$$k = \frac{d^2\varphi}{12{\tau_h}^2}, \quad (10)$$

$$F = \frac{{\tau_e}^2}{\varphi}, \tag{11}$$

where d is the aperture, ${\tau_h}^2$ is hydraulic tortuosity, ${\tau_e}^2$ is electrical tortuosity, and φ is porosity. Porosity can be assumed to equal 1 in the calculation of the fracture permeability, and it equals d/n_z in the calculation of the formation factor under the assumption of a very small matrix porosity. We used the mean aperture and calculated tortuosities to predict the fracture permeability from Eq. (10) and the formation factor from Eq. (11), which are plotted in Fig. 9 along with their simulated values. The simulated and predicted values of fracture permeability are in good agreement for mean apertures larger than 0.1 mm (Fig. 9a). The slight difference between simulated and predicted permeability may arise from the discrepancy between the mean aperture and the actual hydraulic flow width, i.e., hydraulic aperture (Brown, 1989). The predicted and simulated values of formation factor also match for mean apertures larger than 0.1 mm (Fig. 9b), if the predicted value is divided by 7 to adjust the offset. This offset may represent the difference between the mean aperture and the actual width of the electrical conduction channel (i.e., electric aperture). As pointed out by Brown (1989), the use of mean aperture would not reproduce the absolute value of the electric current, which is affected by higher values of the local electric current in smaller local apertures (Fig. 6c). Even a weighted harmonic mean of the local aperture over the cell cannot explain this discrepancy (Fig. E1 in Appendix E); therefore, the difference between the mean aperture and electric aperture (i.e., the predicted and simulated formation factors) is an inherent reflection of the local connectivity of electric paths, which cannot be characterized from the aperture alone (Appendix E).

The agreement between simulated and predicted results for mean apertures greater than 0.1 mm indicates that the equivalent channel model enables us to consider the roughness effect by taking tortuosity into account, a capability lacking in the parallel-plate model. However, both predicted results by Eqs. (10) and (11) deviate from the simulation results at mean apertures smaller than 0.1 mm. These features may be unrealistic and a consequence of the smaller number of flow paths at small apertures (Figs. 4i–l and 6i–l). Simulations with higher resolution might resolve these discrepancies; in fact, when

368 the simulation uses smaller voxel sizes, hydraulic tortuosity continuously increases as the aperture
369 decreases, and the permeability predicted from tortuosity is closely consistent with simulation results
370 (Fig. B2b) above a percolation threshold, as discussed in section 4.2. However, the computational cost
371 is prohibitive at present. Given the strong trend of the hydraulic and electrical tortuosities with apertures
372 greater than 0.1 mm, we conclude that these unrealistic results at smaller mean apertures do not affect
373 the overall discussion. We note that the permeability and formation factor are successfully calculated
374 with high repeatability; hence, the results for these global transport properties are reliable.
375
376 **4.2 Relationship between hydraulic and electrical properties**
377 We have established that changes in hydraulic properties (fracture permeability and flow area) and
378 electrical properties (formation factor or resistivity) with respect to the mean aperture are both
379 independent of fracture length scales at various ranges of contact area (10–65%) and mean aperture
380 (0.05–0.18 mm) (Fig. 7). These scale-independent characteristics arise from the scaleless changes of the
381 tortuosity (Fig. 8), which may be a key factor controlling those scaleless properties. Although the
382 decrease of the mean aperture mimics the aperture closure caused by stress increase (Fig. 3), these
383 changes in transport properties with mean aperture might not precisely match the corresponding changes
384 with stress increase. However, because scale-independent changes of fracture permeability and flow
385 area with stress changes were also reported by Ishibashi et al. (2015) in laboratory experiments with
386 mated fractures, our observed scale-independent characteristics should not have significant differences
387 from those with stress changes. Note that even if their scale dependence with aperture changes differs
388 from their scale dependence with stress changes, their respective relationships with hydraulic and
389 electrical properties should have identical trends, as we discuss below. It should also be noted that these
390 features of scale independence are only confirmed at the present model scales, i.e., in mated fractures
391 with lengths of 24–144 mm.
392 Having explored the scale dependence of each transport property, we then examined the respective
393 correlations of fracture permeability and flow area with formation factor (Fig. 10). The relationship

between fracture permeability and formation factor (*k*–*F* relationship hereafter) plotted in Fig. 10a is scale-independent. The *k*–*F* relationship can be empirically formulated as

$$\log k = -\alpha \cdot \log F - \beta, \tag{12}$$

where α and β are empirical parameters depending on ranges of permeability, for example, α = 1.0 and β = 8.0 when $k < 10^{-10.8}$ m^2, whereas α = 1.8 and β = 5.7 when $k > 10^{-10.8}$ m^2 (Fig. 10). Although the stochastic process of the fracture modeling produces small fluctuations of the *k*–*F* relationships when the aperture is small (up to 16% relative error), the values of α and β are not changed significantly by stochastic fluctuations (Fig. D3 in Appendix D). The slope α is related to the sensitivity to the tortuosity from the equivalent channel model (Appendix F), expressed by the slope ε of the log-log relationship between the tortuosity and the mean aperture in Fig. 8:

$$\alpha = \frac{2-\varepsilon}{1-\varepsilon}. \tag{13}$$

It appears that α is bounded between values of 1 and 2. The tortuosity change is very sensitive to aperture change at higher values of α and insensitive to aperture closure at lower values (Brace, 1989).

As the present results are based on mated single fractures, let us consider the case of multiple fractures, which is more realistic in geothermal fields. Assuming a vertical series of single fractures having the same fractal surfaces in a unit volume, the resultant permeability and formation factor are characterized by the simple summation of the aperture (multiplication of the number of fractures and mean aperture) based on Eqs. (10) and (11). In the case of 10 fractures, permeability is higher than the present results by two orders of magnitude, whereas the formation factor decreases by one order. The empirical parameter β is thus influenced by the number of fractures in a unit volume (i.e., fracture density), whereas the slope α remains constant regardless of the fracture density. The offset β can be neglected for monitoring purposes as

$$\frac{k}{k'} = \frac{F}{F'}^{-\alpha}, \tag{14}$$

where k' and F' are arbitrary reference values of the permeability and formation factor, respectively. Overall, the *k*–*F* relationship is scale-independent whereas the slope α remains constant regardless of the fracture length scale and roughness.

The relationship between the flow area and the formation factor also displays scale independence (Fig. 10b). This potentially arises from the scale independence of flow area and permeability (Fig. 7) and the *k*–*F* relationship (Fig. 10a).

The *k*–*F* relationship shows a transition at a specific fracture permeability, indicating that the empirical parameters α and β are not constant at all permeability values. Because the decrease of permeability is associated with the evolution of stagnant flow and high tortuosity due to aperture closure, changes in the *k*–*F* relationship may be related to changes in local transport properties. Figure 11 schematically summarizes the changes in the formation factor, tortuosity, mean aperture, and stagnant area against fracture permeability. Note that only the tortuosities for $k < 10^{-10}$ were simulated (Fig. 8), whereas tortuosities for $k > 10^{-10}$ were calculated by using the corresponding mean apertures and α from Eq. (13) as a reference value. The three panels at the bottom of Fig. 11 illustrate the associated changes of the hydraulic and electrical paths, composed by overlaying the flow channels selected from Figs. 4a–c and 5a–c. The trends of the *k*–*F* relationships are divided on the basis of the flow channels into two stages: the connected region and the less-connected region. In the connected region ($k > 10^{-10.8}$ in this study), decreasing aperture (or the increase of contacting asperities) affects the local tortuosity which in turn controls the effect of roughness on fracture permeability and formation factor (Fig. 9). As the tortuosity constantly increases with aperture closure (Fig. 8), the trend of the *k*–*F* relationship remains constant (Fig. 10). The stagnant area gradually increases as long as the flow channels are connected (Figs. 4b, e, h, k). In the less-connected region ($k < 10^{-10.8}$), the *k*–*F* relationship shows a steeper slope (Fig. 10), indicating that tortuosity has nearly stopped increasing. The stagnant area also reaches a peak at this stage because of the disconnection of the flow paths (Figs. 4c, f, i, l). Because the formation factor mainly depends on the tortuosity (Eq. (11)), its rate of change slightly decreases. In contrast, the fracture permeability responds to the combination of the tortuosity and aperture changes

by continuously decreasing (Eq. (10)). Thus, the division of the *k–F* relationship may reflect the changes in local flow behavior associated with changes in the tortuosity and connectivity of path channels. This inflection point of the *k–F* relationship may correspond to a percolation threshold at which the flow paths become disconnected (Fig. 11).

4.3 Implications for geothermal field monitoring

The different trends of the *k–F* relationships in the connected and less-connected regions indicate the difference in the sensitivity of resistivity to changes in permeability in response to the connectivity within subsurface fractures. This means that resistivity monitoring should be able to more readily detect permeability changes in less-connected fractures than in connected fractures. In practice, resistivity observations in Australian EGS projects have detected changes in resistivity of around 5% (Didana et al., 2017) and 10% (Peacock et al., 2013) associated with hydraulic stimulation of pre-existing fault systems. Assuming $\alpha = -1.8$ in Eq. (14), these resistivity changes correspond to 11% and 21% increases in permeability, respectively. Although α is potentially different in rock fracture surfaces with different fractal characteristics, it will take values between 1 and 2 according to Eq. (13); indeed, permeability changes are always larger than observed resistivity changes. However, because our model assumes a simple vertical series of single fractures, the changes in transport properties in intersecting fracture networks (e.g., Kirkby and Heinson, 2017) should be further investigated. Moreover, it should be noted that permeability enhancement by hydraulic stimulation is triggered not only by joint openings but also by shear slips (e.g., Rinaldi and Rutqvist, 2019). Because our digital fracture models are mated fractures based on isotropic surfaces, future work should employ natural rock fractures with anisotropic characteristics (e.g., sheared fractures) to confirm the limitations of our proposed model. We found that empirical parameters in our proposed formula are constant in fractures with the same fractal characteristics, regardless of their length scales. This finding implies that investigations of small-scale fractures are sufficient to study the *k–F* relationship, such that laboratory-scale relationships can be seamlessly extrapolated to fractures in natural settings, even for differing empirical parameters of

fractures at different locations. Because our experimental fracture was much smaller than natural fractures, which may reach the kilometer scale (Didana et al., 2017), future research needs to investigate further scale dependencies and consider the use of more efficient grid systems, such as the multigrid approach.

5. Conclusion

We investigated the changes with aperture closure in the fracture permeability, flow area, and formation factor of mated fractures and used upscaled digital fracture simulations to clarify their scaling behavior. We confirmed that fracture permeability, formation factor, and the relationship between them are scale-independent with respect to the mean aperture. Our digital fracture simulations revealed that hydraulic and electrical properties have slightly different local transport behaviors because of their cubic and linear dependences, respectively, on the aperture. Both hydraulic and electrical properties demonstrate scale-independent behaviors that reflect the scaleless changes of path tortuosity. Notably, we found scale-independent relationships between permeability and formation factor (the *k–F* relationship) and between flow area and formation factor. Our digital fractures with isotropic fractal surfaces successfully reproduced nonlinear *k–F* relationships comparable to those previously observed in natural rock fractures. We demonstrated that the *k–F* relationship could be determined from empirically determined properties regardless of fracture length scale. The *k–F* relationship reflects the changes in the local flow behavior that can be determined from the changes in tortuosity and connectivity of path channels. Although further study is needed to confirm these empirical parameters, our finding of scale independence in the *k–F* relationship indicates that laboratory-scale fracture properties can be confidently used for interpreting field data and for fracture flow monitoring by utilizing data for resistivity, which is remotely observed with geophysical methods.

Acknowledgments

The authors acknowledge I. Katayama (Hiroshima University), K. Kitamura (Kyushu University) and K. Hatakeyama (Hiroshima University) for technical support. Comments from A. Kirkby greatly improved the manuscript. This study was supported in part by the Japan Society for the Promotion of Science (JSPS) through a Grant-in-Aid for JSPS Fellows, JP19J10125 (to K.S.), Grant-in-Aid for Young Scientists, JP19K15100 (to F.J.) and Grant-in-Aid for Challenging Exploratory Research, JP20K20948 (to T.T.). T.T., F.J., and O.N. are also grateful for the support of the International Institute for Carbon Neutral Energy Research (I2CNER), which is sponsored by the World Premier International Research Center Initiative of the Ministry of Education, Culture, Sports, Science and Technology (MEXT), Japan.

References

Abdelfettah, Y., Sailhac, P., Larnier, H., Matthey, P.D., Schill, E., 2018. Continuous and time-lapse magnetotelluric monitoring of low volume injection at Rittershoffen geothermal project, northern Alsace – France. Geothermics 71, 1–11. https://doi.org/10.1016/j.geothermics.2017.08.004

Ahrenholz, B., Tölke, J., Lehmann, P., Peters, A., Kaestner, A., Krafczyk, M., Durner, W., 2008. Prediction of capillary hysteresis in a porous material using lattice-Boltzmann methods and comparison to experimental data and a morphological pore network model. Adv. Water Resour. 31, 1151–1173. https://doi.org/10.1016/j.advwatres.2008.03.009

Aizawa, K., Kanda, W., Ogawa, Y., Iguchi, M., Yokoo, A., Yakiwara, H., Sugano, T., 2011. Temporal changes in electrical resistivity at Sakurajima volcano from continuous magnetotelluric observations. J. Volcanol. Geotherm. Res. 199, 165–175. https://doi.org/10.1016/j.jvolgeores.2010.11.003

Andrä, H., Combaret, N., Dvorkin, J., Glatt, E., Han, J., Kabel, M., Keehm, Y., Krzikalla, F., Lee, M., Madonna, C., Marsh, M., Mukerji, T., Saenger, E.H., Sain, R., Saxena, N., Ricker, S., Wiegmann, A., Zhan, X., 2013. Digital rock physics benchmarks—Part I: Imaging and segmentation. Comput. Geosci. 50, 25–32. https://doi.org/10.1016/j.cageo.2012.09.005

Archie, G.E., 1942. The Electrical Resistivity Log as an Aid in Determining Some Reservoir Characteristics. Trans. AIME 146, 54–62. https://doi.org/10.2118/942054-G

519 Bahat, D., Engelder, T., 1984. Surface morphology on cross-fold joints of the Appalachian Plateau,
520 New York and Pennsylvania. Tectonophysics 104, 299–313. https://doi.org/10.1016/0040-
521 1951(84)90128-8

522 Brown, S.R., 1987. Fluid flow through rock joints: The effect of surface roughness. J. Geophys. Res.
523 92, 1337–1347. https://doi.org/10.1029/JB092iB02p01337

524 Brown, S.R., 1989. Transport of fluid and electric current through a single fracture. J. Geophys. Res.
525 94, 9429. https://doi.org/10.1029/JB094iB07p09429

526 Brown, S.R., 1995. Simple mathematical model of a rough fracture. J. Geophys. Res. Solid Earth 100,
527 5941–5952. https://doi.org/10.1029/94JB03262

528 Brown, S.R., Caprihan, A., Hardy, R., 1998. Experimental observation of fluid flow channels in a
529 single fracture. J. Geophys. Res. Solid Earth 103, 5125–5132. https://doi.org/10.1029/97JB03542

530 Brown, S.R., Kranz, R.L., Bonner, B.P., 1986. Correlation between the surfaces of natural rock joints.
531 Geophys. Res. Lett. 13, 1430–1433. https://doi.org/10.1029/GL013i013p01430

532 Brown, S.R., Scholz, C.H., 1985. Broad bandwidth study of the topography of natural rock surfaces. J.
533 Geophys. Res. 90, 12575. https://doi.org/10.1029/JB090iB14p12575

534 Brush, D. J., and Thomson, N. R., 2003. Fluid flow in synthetic rough-walled fractures: Navier-
535 Stokes, Stokes, and local cubic law simulations, Water Resour. Res., 39, 1085.
536 doi:10.1029/2002WR001346

537 Chen, G., Spetzler, H., 1993. Topographic characteristics of laboratory induced shear fractures. Pure
538 Appl. Geophys. PAGEOPH 140, 123–135. https://doi.org/10.1007/BF00876874

539 Didana, Y.L., Heinson, G., Thiel, S., Krieger, L., 2017. Magnetotelluric monitoring of permeability
540 enhancement at enhanced geothermal system project. Geothermics 66, 23–38.
541 https://doi.org/10.1016/j.geothermics.2016.11.005

542 Garboczi E.J., 1998. Finite element and finite difference programs for computing the linear electric
543 and elastic properties of digital image of random materials. Natl Inst Stand Technol Interag Rep
544 6269.

545 Glover, P.W.J., Matsuki, K., Hikima, R., Hayashi, K., 1997. Fluid flow in fractally rough synthetic
546 fractures. Geophys. Res. Lett. 24, 1803–1806. https://doi.org/10.1029/97GL01670

547 Glover, P.W.J., Matsuki, K., Hikima, R., Hayashi, K., 1998a. Fluid flow in synthetic rough fractures
548 and application to the Hachimantai geothermal hot dry rock test site. J. Geophys. Res. Solid
549 Earth 103, 9621–9635. https://doi.org/10.1029/97JB01613

550 Glover, P.W.J., Matsuki, K., Hikima, R., Hayashi, K., 1998b. Synthetic rough fractures in rocks. J.
551 Geophys. Res. Solid Earth 103, 9609–9620. https://doi.org/10.1029/97JB02836

552 Guéguen Y., Palciauskas V., 1994. Introduction to the physics of rocks. Princeton University Press,
553 Princeton.

554 Hata, M., Oshiman, N., Yoshimura, R., Tanaka, Y., Uyeshima, M., 2015. Three-dimensional
555 electromagnetic imaging of upwelling fluids in the Kyushu subduction zone, Japan. J. Geophys.
556 Res. Solid Earth 120, 1–17. https://doi.org/10.1002/2014JB011336

557 Hawkins, A.J., Becker, M.W., Tester, J.W., 2018. Inert and Adsorptive Tracer Tests for Field
558 Measurement of Flow-Wetted Surface Area. Water Resour. Res. 54, 5341–5358.
559 https://doi.org/10.1029/2017WR021910

560 He, X., Luo, L.-S., 1997. Lattice Boltzmann Model for the Incompressible Navier–Stokes Equation. J.
561 Stat. Phys. 88, 927–944. https://doi.org/10.1023/B:JOSS.0000015179.12689.e4

562 Ishibashi, T., Watanabe, N., Hirano, N., Okamoto, A., Tsuchiya, N., 2015. Beyond-laboratory-scale
563 prediction for channeling flows through subsurface rock fractures with heterogeneous aperture
564 distributions revealed by laboratory evaluation. J. Geophys. Res. Solid Earth 120, 106–124.
565 https://doi.org/10.1002/2014JB011555

566 Jackson, D.B., Kauahikaua, J., Zablocki, C.J., 1985. Resistivity monitoring of an active volcano using
567 the controlled-source electromagnetic technique: Kilauea, Hawaii. J. Geophys. Res. 90, 12545–
568 12555. https://doi.org/10.1029/JB090iB14p12545

569 Jaeger, J., Cook, N.G., Zimmerman, R., 2007. Fundamentals of Rock Mechanics, 4th ed. Wiley–
570 Blackwell, New Jersey.

571 Jiang, F., Tsuji, T., Hu, C., 2014. Elucidating the Role of Interfacial Tension for Hydrological
572 Properties of Two-Phase Flow in Natural Sandstone by an Improved Lattice Boltzmann Method.
573 Transp. Porous Media 104, 205–229. https://doi.org/10.1007/s11242-014-0329-0

574 Kirkby, A., and Heinson, G., 2017. Three-dimensional resistor network modeling of the resistivity and
575 permeability of fractured rocks, J. Geophys. Res. Solid Earth, 122, 2653–2669.
576 doi:10.1002/2016JB013854

Kirkby, A., Heinson, G., Krieger, L., 2016. Relating permeability and electrical resistivity in fractures using random resistor network models. J. Geophys. Res. Solid Earth 121, 1546–1564. https://doi.org/10.1002/2015JB012541

Kranz, R.L., Frankel, A.D., Engelder, T., Scholz, C.H., 1979. The permeability of whole and jointed Barre Granite. Int. J. Rock Mech. Min. Sci. Geomech. Abstr. 16, 225–234. https://doi.org/10.1016/0148-9062(79)91197-5

Maithya, J., Fujimitsu, Y., 2019. Analysis and interpretation of magnetotelluric data in characterization of geothermal resource in Eburru geothermal field, Kenya. Geothermics 81, 12–31. https://doi.org/10.1016/j.geothermics.2019.04.003

Matsuki, K., Chida, Y., Sakaguchi, K., Glover, P.W.J., 2006. Size effect on aperture and permeability of a fracture as estimated in large synthetic fractures. Int. J. Rock Mech. Min. Sci. 43, 726–755. https://doi.org/10.1016/j.ijrmms.2005.12.001

Mogi, T., Nakama, S., 1993. Magnetotelluric interpretation of the geothermal system of the Kuju volcano, southwest Japan. J. Volcanol. Geotherm. Res. 56, 297–308. https://doi.org/10.1016/0377-0273(93)90022-J

Nemoto, K., Watanabe, N., Hirano, N., Tsuchiya, N., 2009. Direct measurement of contact area and stress dependence of anisotropic flow through rock fracture with heterogeneous aperture distribution. Earth Planet. Sci. Lett. 281, 81–87. https://doi.org/10.1016/j.epsl.2009.02.005

Neuville, A., Toussaint, R., Schmittbuhl, J., 2010. Fracture roughness and thermal exchange: A case study at Soultz-sous-Forêts. Comptes Rendus Geosci. 342, 616–625. https://doi.org/10.1016/j.crte.2009.03.006

Ogilvie, S.R., Isakov, E., Glover, P.W.J., 2006. Fluid flow through rough fractures in rocks. II: A new matching model for rough rock fractures. Earth Planet. Sci. Lett. 241, 454–465. https://doi.org/10.1016/j.epsl.2005.11.041

Okoroafor, E.R., Horne, R.N., 2019. Thermal Performance Implications of Flow Orientation Relative to Fracture Shear Offset in Enhanced Geothermal Systems, in: Proceedings of the 44th Workshop on Geothermal Reservoir Engineering, Stanford University, Stanford, California, SGP-TR-214.

Olsson, W.A., Brown, S.R., 1993. Hydromechanical response of a fracture undergoing compression and shear. Int. J. Rock Mech. Min. Sci. Geomech. Abstr. 30, 845–851. https://doi.org/10.1016/0148-9062(93)90034-B

608 Paterson, M.S., 1983. The equivalent channel model for permeability and resistivity in fluid-saturated
609 rock—A re-appraisal. Mech. Mater. 2, 345–352. https://doi.org/10.1016/0167-6636(83)90025-X

610 Peacock, J.R., Thiel, S., Reid, P., Heinson, G., 2012. Magnetotelluric monitoring of a fluid injection:
611 Example from an enhanced geothermal system. Geophys. Res. Lett. 39, 3–7.
612 https://doi.org/10.1029/2012GL053080

613 Peacock, J.R., Thiel, S., Heinson, G.S., Reid, P., 2013. Time-lapse magnetotelluric monitoring of an
614 enhanced geothermal system. GEOPHYSICS 78, B121–B130. https://doi.org/10.1190/geo2012-
615 0275.1

616 Power, W.L., Durham, W.B., 1997. Topography of natural and artificial fractures in granitic rocks:
617 Implications for studies of rock friction and fluid migration. Int. J. Rock Mech. Min. Sci. 34,
618 979–989. https://doi.org/10.1016/S1365-1609(97)80007-X

619 Power, W.L., Tullis, T.E., Brown, S.R., Boitnott, G.N., Scholz, C.H., 1987. Roughness of natural fault
620 surfaces. Geophys. Res. Lett. 14, 29–32. https://doi.org/10.1029/GL014i001p00029

621 Pyrak-Nolte, L.J., Cook, N.G.W., Nolte, D.D., 1988. Fluid percolation through single fractures.
622 Geophys. Res. Lett. 15, 1247–1250. https://doi.org/10.1029/GL015i011p01247

623 Raven, K.G., Gale, J.E., 1985. Water flow in a natural rock fracture as a function of stress and sample
624 size. Int. J. Rock Mech. Min. Sci. Geomech. Abstr. 22, 251–261. https://doi.org/10.1016/0148-
625 9062(85)92952-3

626 Rinaldi, A.P., Rutqvist, J., 2019. Joint opening or hydroshearing? Analyzing a fracture zone
627 stimulation at Fenton Hill. Geothermics 77, 83–98.
628 https://doi.org/10.1016/j.geothermics.2018.08.006

629 Sausse, J., 2002. Hydromechanical properties and alteration of natural fracture surfaces in the Soultz
630 granite (Bas-Rhin, France). Tectonophysics 348, 169–185. https://doi.org/10.1016/S0040-
631 1951(01)00255-4

632 Sawayama, K., Ishibashi, T., Jiang, F., Tsuji, T., and Fujimitsu, Y., 2020. Relating Hydraulic-
633 Electrical-Elastic Properties of Natural Rock Fractures at Elevated Stress and Associated
634 Transient Changes of Fracture Flow. Preprint on Earth and Space Science Open Archive.
635 https://doi.org/10.1002/essoar.10502423.1

636 Sawayama, K., Kitamura, K., Fujimitsu, Y., 2018a. Laboratory measurements on electric and elastic
637 properties of fractured geothermal reservoir rocks under simulated EGS conditions. GRC
638 Transactions 42, 2459–2475.

Sawayama, K., Kitamura, K., Fujimitsu, Y., 2018b. Relationship between Complex Resistivity, Elastic Wave and Water Saturation of Cracked Andesite under Laboratory Fluid-Flow Test. BUTSURI-TANSA(Geophysical Exploration) 71, 71–85 [in Japanese with English abstract]. https://doi.org/10.3124/segj.71.71

Sawayama, K., Kitamura, K., Fujimitsu, Y., 2019. Effects of water saturation, fracture and salinity on electric and elastic properties of fractured geothermal rocks. J. Geotherm. Res. Soc. Japan 41, 53–59. https://doi.org/10.11367/grsj.41.53

Saxena, N., Mavko, G., 2016. Estimating elastic moduli of rocks from thin sections: Digital rock study of 3D properties from 2D images. Comput. Geosci. 88, 9–21. https://doi.org/10.1016/j.cageo.2015.12.008

Schultz, R.A., Soliva, R., Fossen, H., Okubo, C.H., Reeves, D.M., 2008. Dependence of displacement–length scaling relations for fractures and deformation bands on the volumetric changes across them. J. Struct. Geol. 30, 1405–1411. https://doi.org/10.1016/j.jsg.2008.08.001

Singurindy, O., Berkowitz, B., 2005. The role of fractures on coupled dissolution and precipitation patterns in carbonate rocks. Adv. Water Resour. 28, 507–521. https://doi.org/10.1016/j.advwatres.2005.01.002

Spengler, R. W., M. P. Chornak, 1984. Stratigraphic and structural characteristics of volcanic rocks in core hole USW G-4, Yucca Mountain, Nye County, Nevada, with a section on geophysical logs by D. C. Muller, and J. Kibler, U. S. Geol. Surv. Open File Rep84-789.

Stesky, R.M., 1986. Electrical conductivity of brine-saturated fractured rock. GEOPHYSICS 51, 1585–1593. https://doi.org/10.1190/1.1442209

Thompson, M.E., Brown, S.R., 1991. The effect of anisotropic surface roughness on flow and transport in fractures. J. Geophys. Res. Solid Earth 96, 21923–21932. https://doi.org/10.1029/91JB02252

Tsang, C., Neretnieks, I., 1998. Flow channeling in heterogeneous fractured rocks. Rev. Geophys. 36, 275–298. https://doi.org/10.1029/97RG03319

Tsang, Y.W., Tsang, C.F., 1987. Channel model of flow through fractured media. Water Resour. Res. 23, 467–479. https://doi.org/10.1029/WR023i003p00467

Tsang, Y.W., Witherspoon, P.A., 1981. Hydromechanical behavior of a deformable rock fracture subject to normal stress. J. Geophys. Res. Solid Earth 86, 9287–9298. https://doi.org/10.1029/JB086iB10p09287

Tsukamoto, K., Aizawa, K., Chiba, K., Kanda, W., Uyeshima, M., Koyama, T., Utsugi, M., Seki, K., Kishita, T., 2018. Three-Dimensional Resistivity Structure of Iwo-Yama Volcano, Kirishima Volcanic Complex, Japan: Relationship to Shallow Seismicity, Surface Uplift, and a Small Phreatic Eruption. Geophys. Res. Lett. 45, 12,821–12,828. https://doi.org/10.1029/2018GL080202

Vogler, D., Settgast, R.R., Annavarapu, C., Madonna, C., Bayer, P., Amann, F., 2018. Experiments and Simulations of Fully Hydro-Mechanically Coupled Response of Rough Fractures Exposed to High-Pressure Fluid Injection. J. Geophys. Res. Solid Earth 123, 1186–1200. https://doi.org/10.1002/2017JB015057

Walsh, J.B., Brace, W.F., 1984. The effect of pressure on porosity and the transport properties of rock. J. Geophys. Res. 89, 9425–9431. https://doi.org/10.1029/JB089iB11p09425

Watanabe, N., Hirano, N., Tsuchiya, N., 2008. Determination of aperture structure and fluid flow in a rock fracture by high-resolution numerical modeling on the basis of a flow-through experiment under confining pressure. Water Resour. Res. 44, 1–11. https://doi.org/10.1029/2006WR005411

Watanabe, N., Hirano, N., Tsuchiya, N., 2009. Diversity of channeling flow in heterogeneous aperture distribution inferred from integrated experimental-numerical analysis on flow through shear fracture in granite. J. Geophys. Res. 114, B04208. https://doi.org/10.1029/2008JB005959

Witherspoon, P.A., Amick, C.H., Gale, J.E., Iwai, K., 1979. Observations of a potential size effect in experimental determination of the hydraulic properties of fractures. Water Resour. Res. 15, 1142–1146. https://doi.org/10.1029/WR015i005p01142

Witherspoon, P.A., Wang, J.S.Y., Iwai, K., Gale, J.E., 1980. Validity of Cubic Law for fluid flow in a deformable rock fracture. Water Resour. Res. 16, 1016–1024. https://doi.org/10.1029/WR016i006p01016

Zimmerman, R.W., Kumar, S. and Bodvarsson, G.S., 1991. Lubrication theory analysis of the permeability of rough-walled fractures. Int. J. Rock Mech. 28, 325–331. https://doi.org/10.1016/0148-9062(91)90597-F

Figures and Tables.

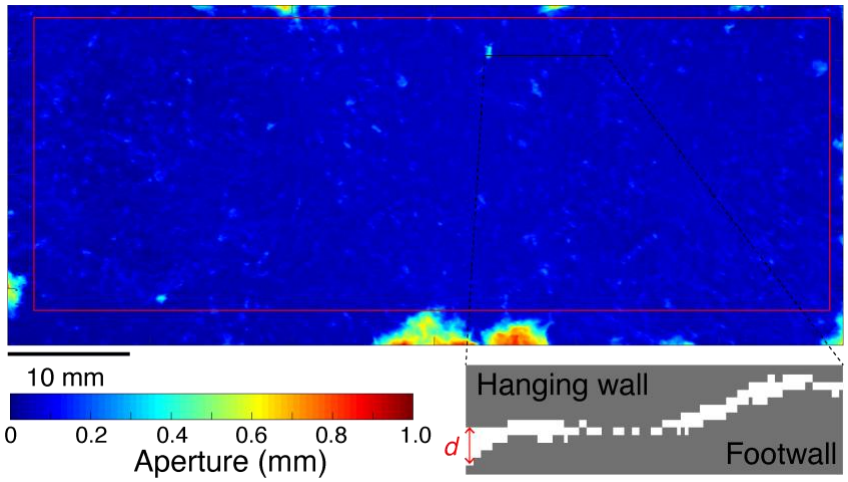

Fig. 1 Image of the fracture surface of the experimental specimen showing the observed initial fracture aperture and a corresponding cross section of the fracture at the location of the black solid line. The white grid cells in the cross section represent the local aperture *d*. The area inside the red outline was used for spectral analysis, excluding the contaminated debris at the edges of the specimen.

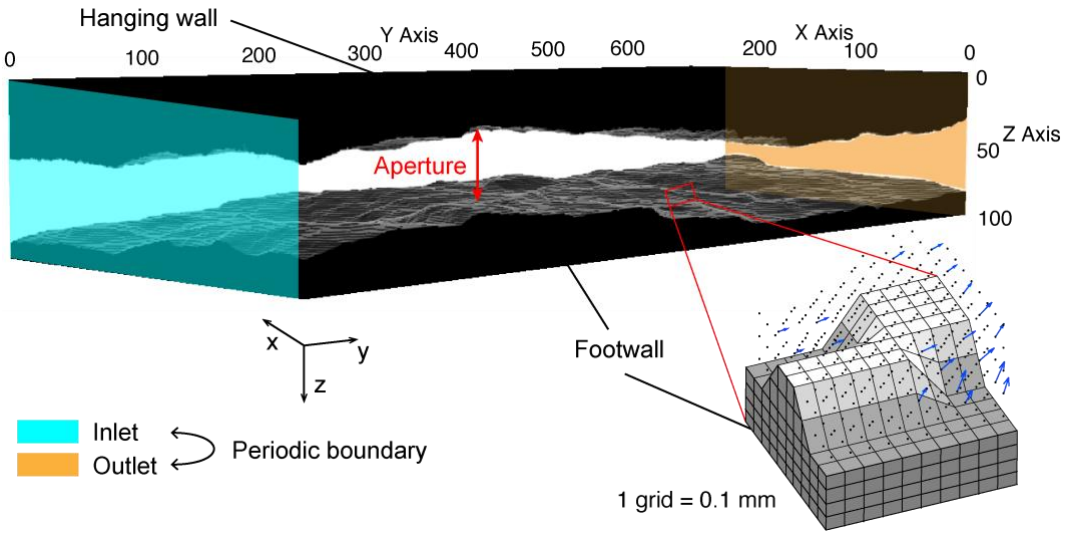

Fig. 2 Three-dimensional digital model of the experimental rock fracture (top) and model setup of the numerical simulation (lower right). The fluid flow and applied voltage are parallel to the fracture plane. A periodic boundary condition was adopted for both the lattice Boltzmann simulation and finite-element modeling. The black points in the model represent grid points; blue arrows are representative flow vectors calculated in each grid cell.

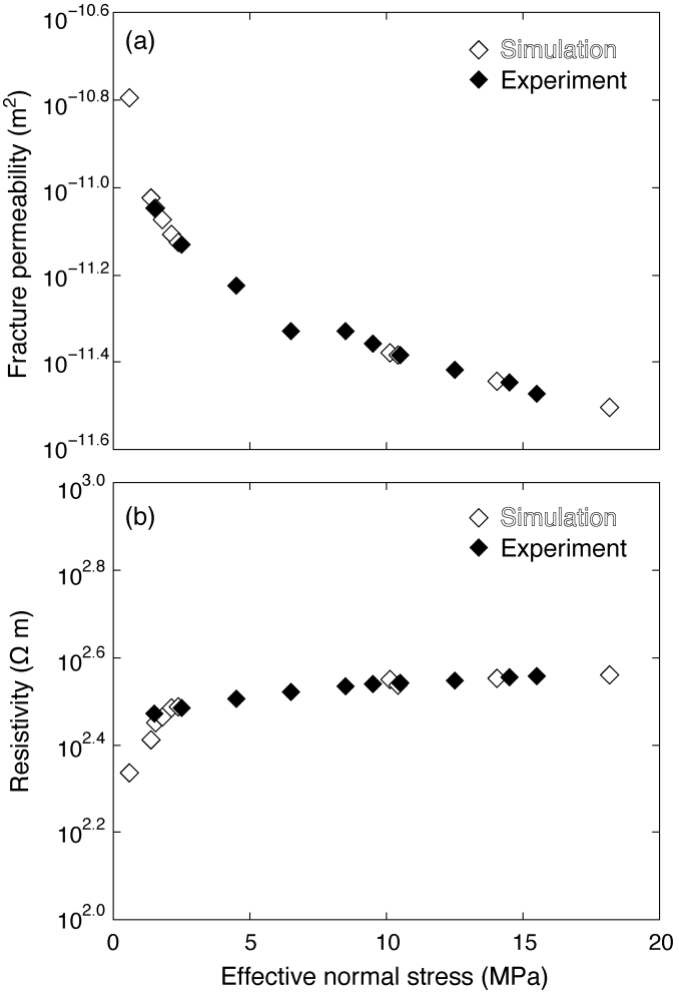

711

712 Fig. 3 Experimental and simulated (a) fracture permeability and (b) resistivity with increasing

713 effective normal stress. Solid and open symbols represent experimental and simulated results,

714 respectively.

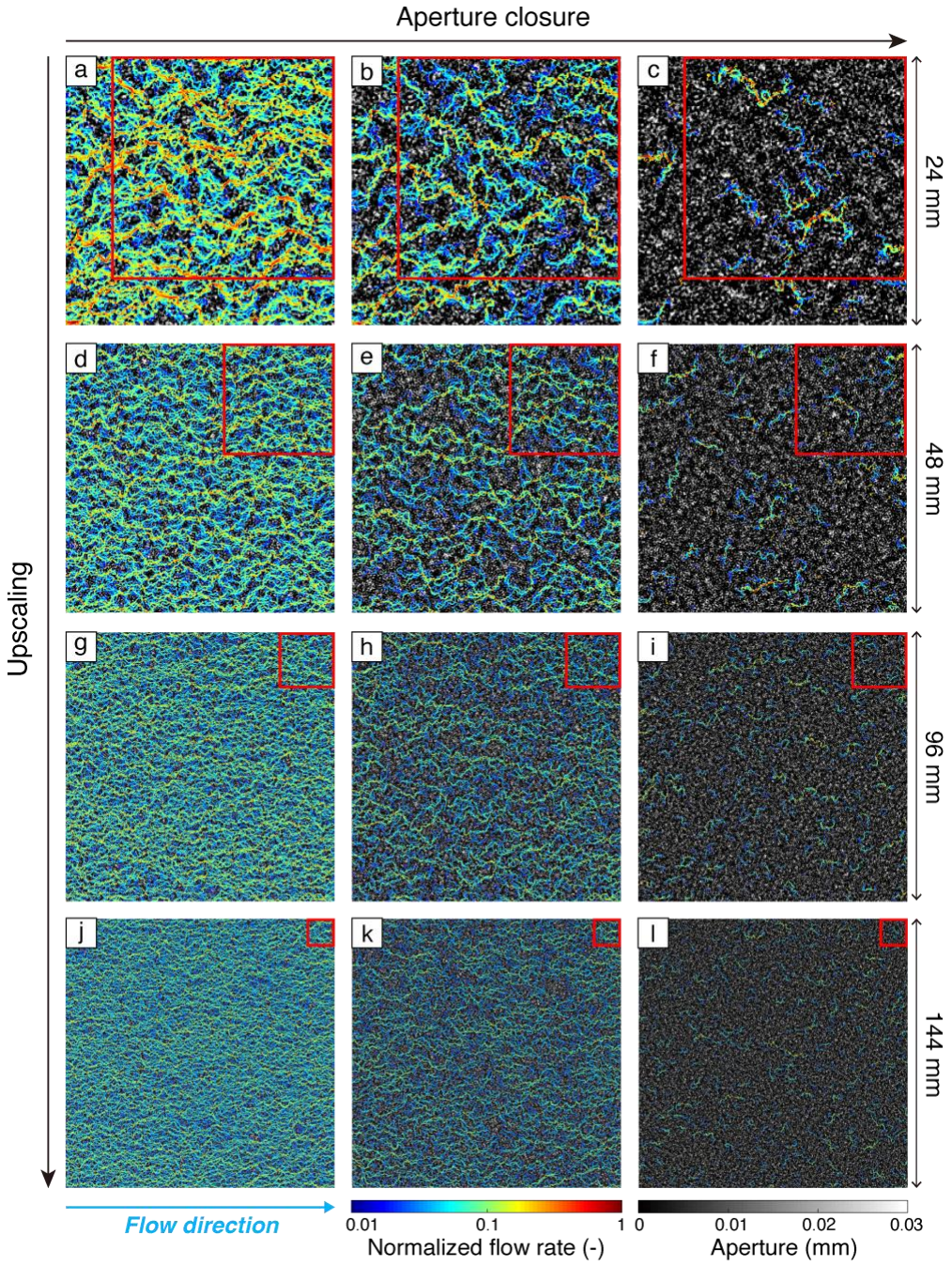

Fig. 4 Simulated fluid flow channels (colors) projected on maps of simulated fracture roughness (grayscale) at three different degrees of aperture closure and four different sample scales: (a–c) 24 mm, (d–f) 48 mm, (g–i) 96 mm, and (j–l) 144 mm. The normalized flow rate represents the vertical summation of flow rates in every z-direction (perpendicular to the fracture plane), normalized by the maximum value in each plot. Colorless regions have flow rates less than 1% of the maximum. Mean apertures are 0.12 mm, 0.085–0.087 mm, and 0.058–0.062 mm in the left, middle, and right columns, respectively.

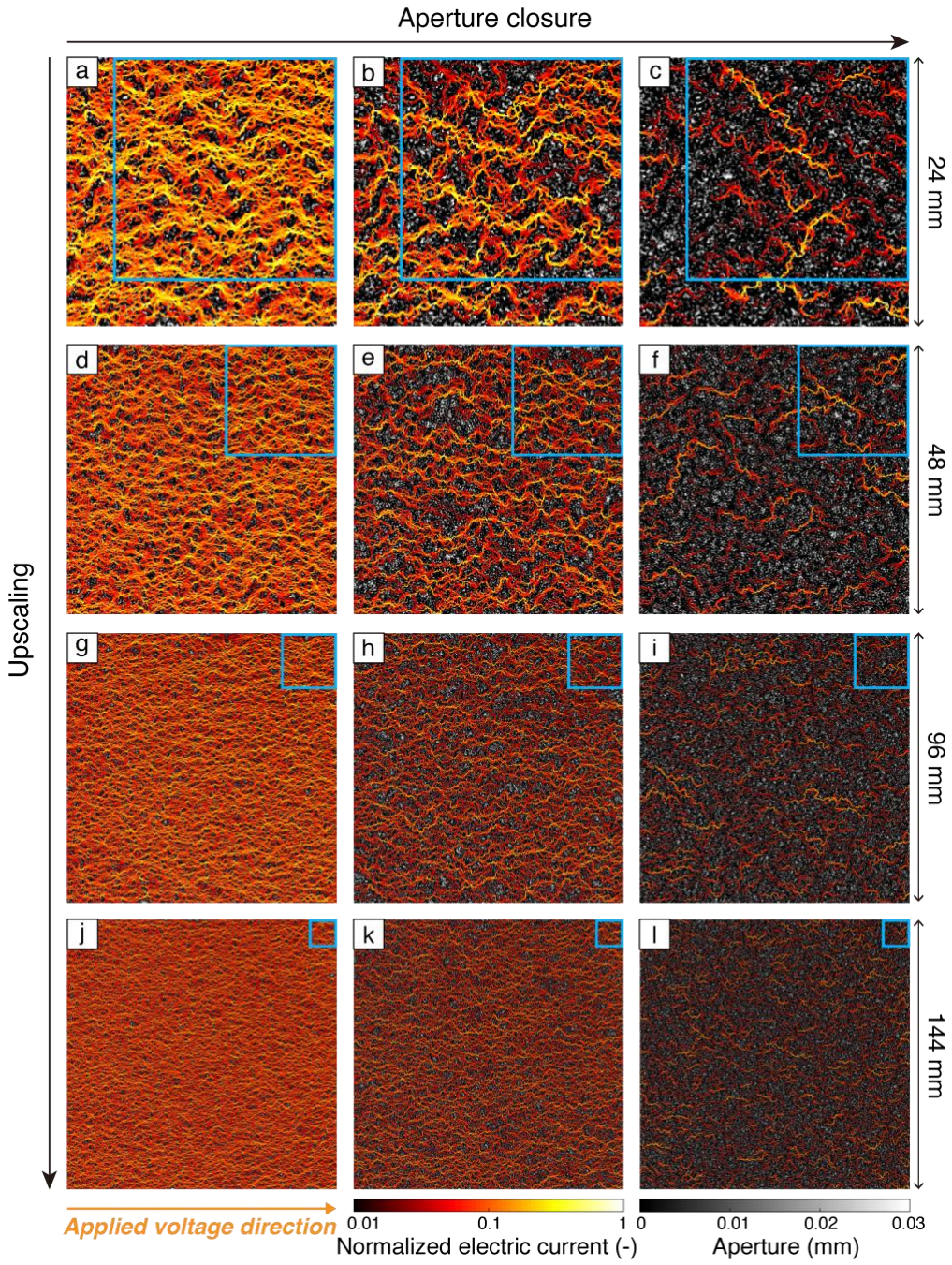

723

724 Fig. 5 Simulated electric current channels (color) projected on maps of simulated fracture
725 roughness (grayscale) at three different degrees of aperture closure and four different sample
726 scales: (a–c) 24 mm, (d–f) 48 mm, (g–i) 96 mm, and (j–l) 144 mm. The normalized electric
727 current represents the vertical summation of the current in every z-direction normalized by
728 the maximum value in each plot. Mean apertures are the same as in Fig. 4.

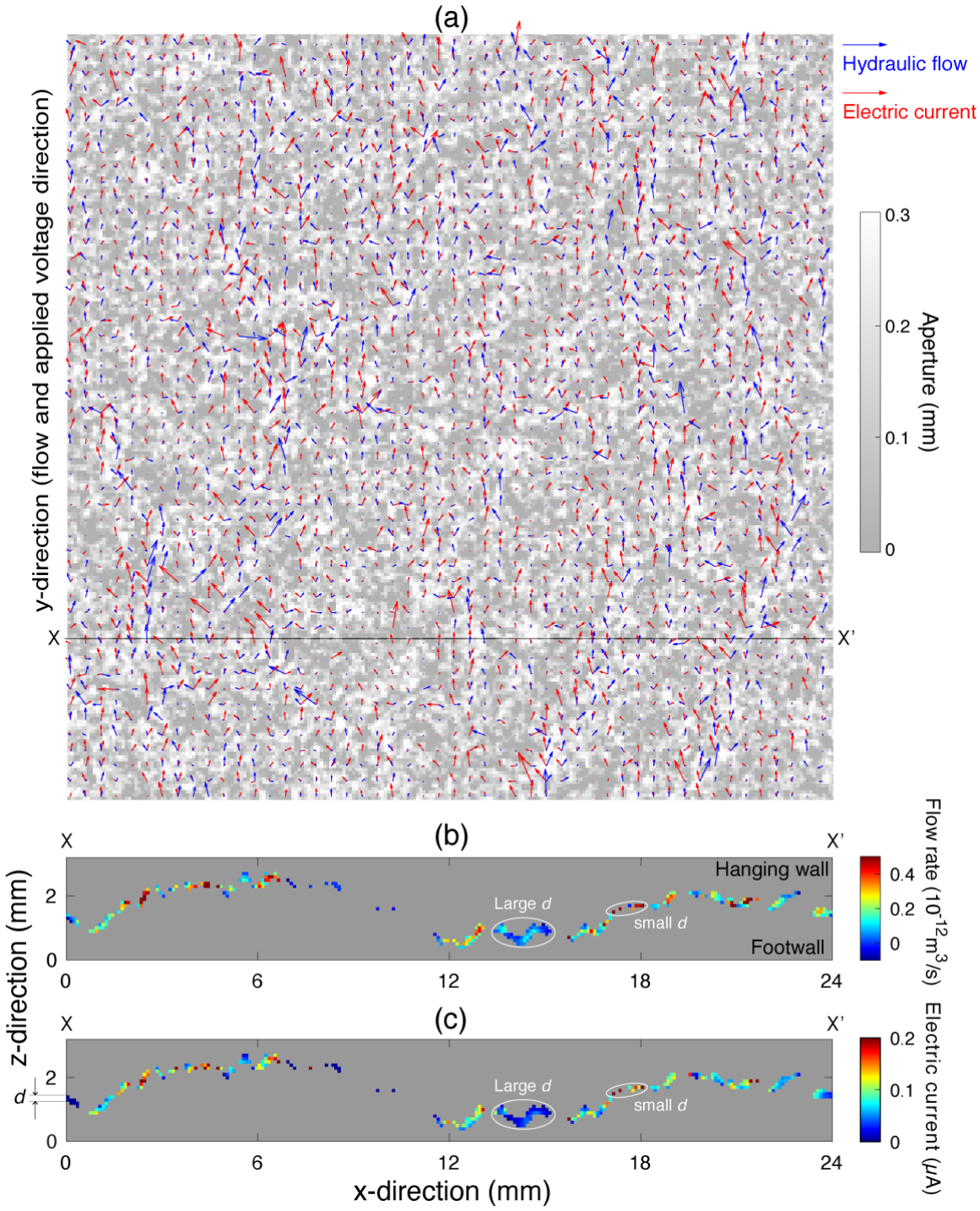

Fig. 6 (a) Map of the local fracture aperture *d* (grayscale) showing streamlines for hydraulic flow (blue) and electrical flow (red). The map is 24 mm square and the mean aperture is 0.11 mm. (b) Cross-sectional profile on line X–X′ showing the hydraulic flow in the fracture. (c) Cross-sectional profile on line X–X′ showing the electrical flow in the fracture. Note that some high-flux channels in both flow rate and electric current appear in narrow apertures, and some low-flux channels appear in wide apertures.

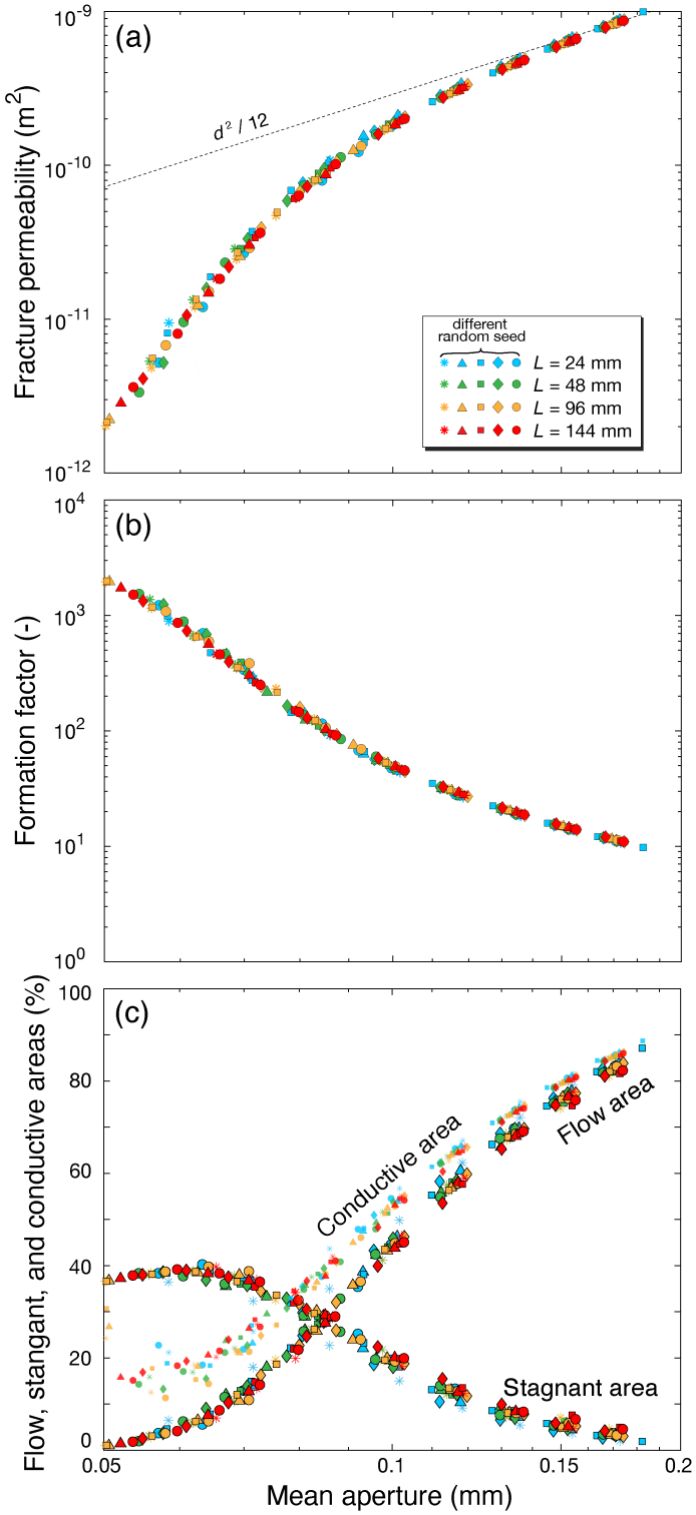

Fig. 7 Changes of (a) fracture permeability, (b) formation factor, and (c) flow, stagnant, and conductive areas as functions of the mean aperture. Symbol shapes correspond to the different random seeds, and their colors correspond to the different fracture length scales. The dashed reference line in (a) denotes a slope of $d^2/12$.

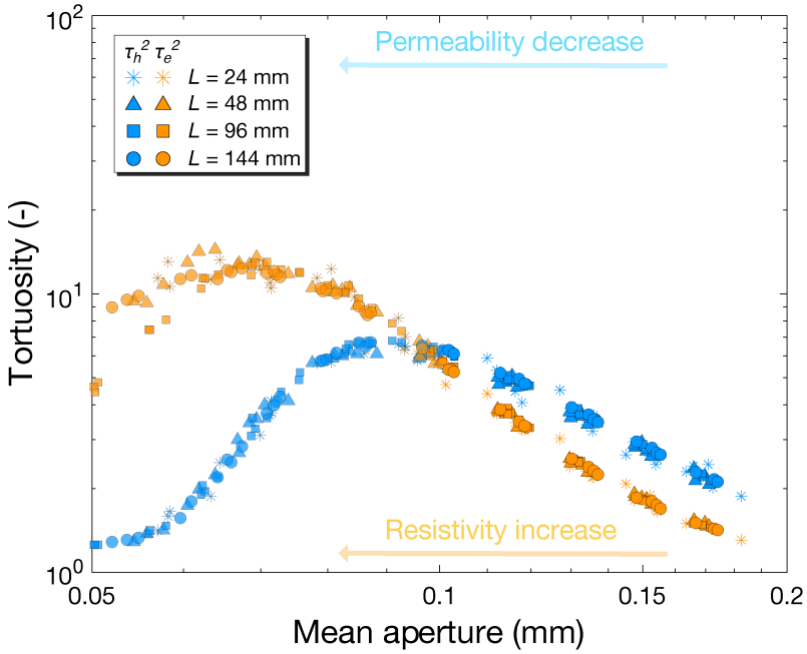

741

742 Fig. 8 Tortuosity of hydraulic flow paths (blue) and electrical flow paths (orange) as a function of

743 mean aperture. Symbol shapes denote different fracture length scales.

744

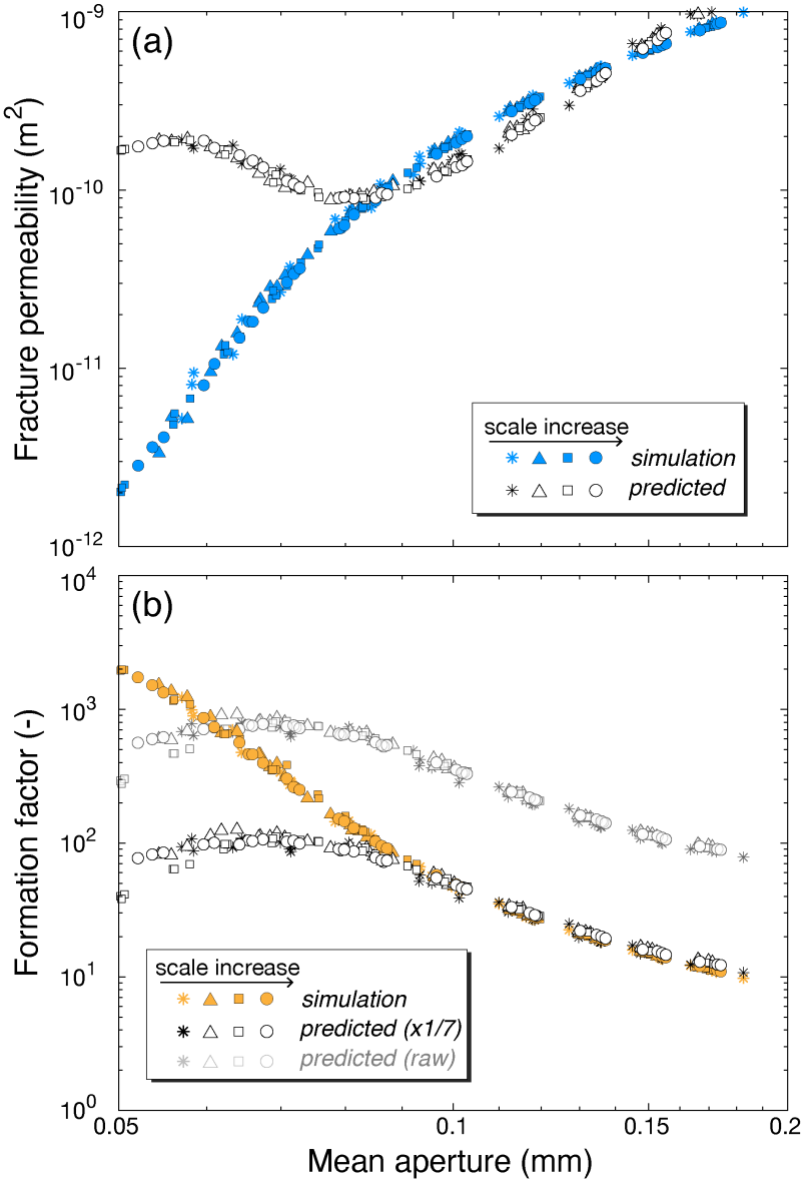

745

746 Fig. 9 Simulated and predicted (a) fracture permeability and (b) formation factor as a function of

747 mean aperture. Symbol shapes represent different fracture length scales; colored and open

748 symbols denote simulated and predicted results, respectively. The predicted formation

749 factor is divided by 7 so that the resultant offset can be adjusted to the simulated results.

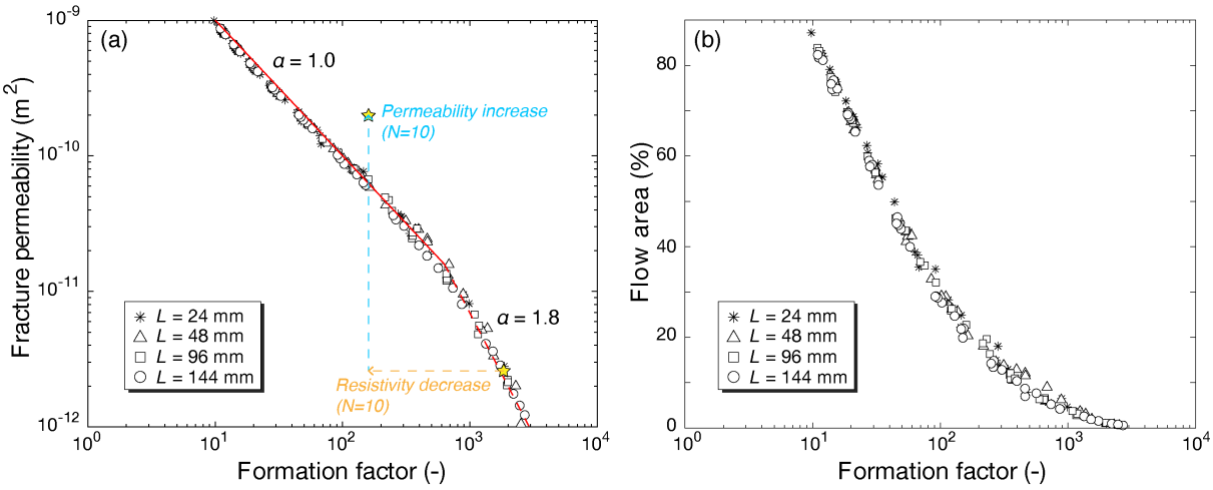

Fig. 10 Graphs of (a) fracture permeability versus formation factor and (b) flow area versus formation factor. Symbol shapes represent different fracture length scales. *N* indicates the number of fractures in a unit volume, and associated changes of permeability and resistivity are illustrated by blue and orange dashed arrows, respectively. Red lines in (a) represent the prediction lines based on Eq. (12) in which α = 1.0 and β = 8.0 for the solid line and α = 1.8 and β = 5.7 for the dashed line.

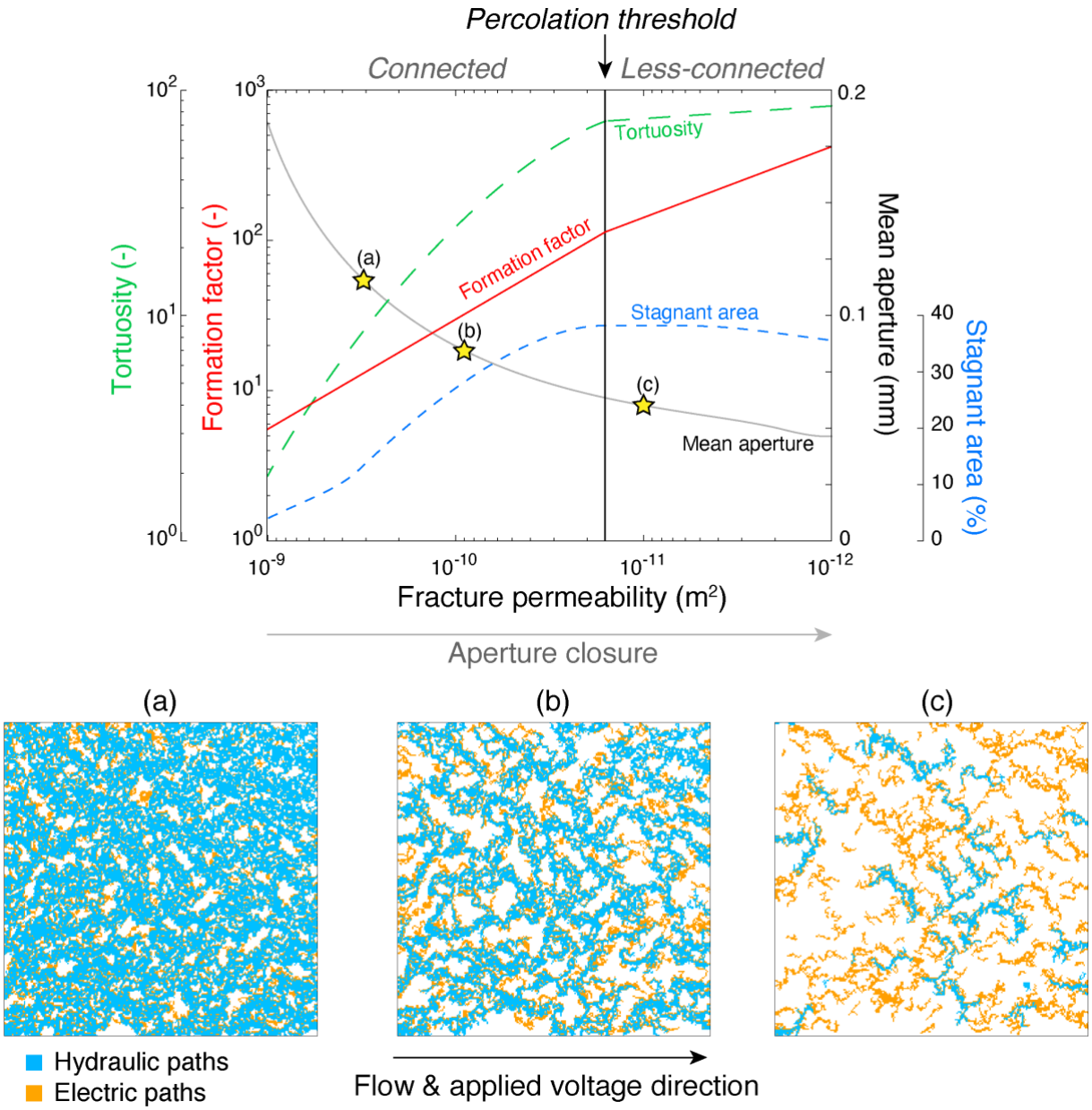

Fig. 11 Schematic plot showing changes in parameters relevant to flow channels as functions of fracture permeability. Points a, b and c are represented by the bottom panels illustrating typical flow channel networks of hydraulic paths (blue) and electrical paths (orange) for the connected and less-connected regions (see text for discussion).

Appendix A. Fractal characteristics of fracture surfaces

Figure A1 shows a power spectrum density (PSD) of the footwall, hanging wall, and the initial aperture profiles produced by the surface measurements. From the PSD slopes of the footwall and hanging wall, the fractal dimension D is determined from following equations (Power et al., 1987; Power and Durham, 1997):

$$D = 7 - 2a, \tag{A.1}$$

where a is the PSD slope of the surface height. In Fig. 1b, the dashed line denotes the mismatch length scale λ_c, which is determined from the curvature of the PSD ratio of the surface height to initial aperture; for the wavelength lower than the threshold wavelength, the PSD ratio begins to decrease with a decreasing spatial frequency (Glover et al, 1998b; Matsuki et al., 2006). Table A1 summarizes the previous studies about surface roughness, fractal dimension, and mismatch length scale.

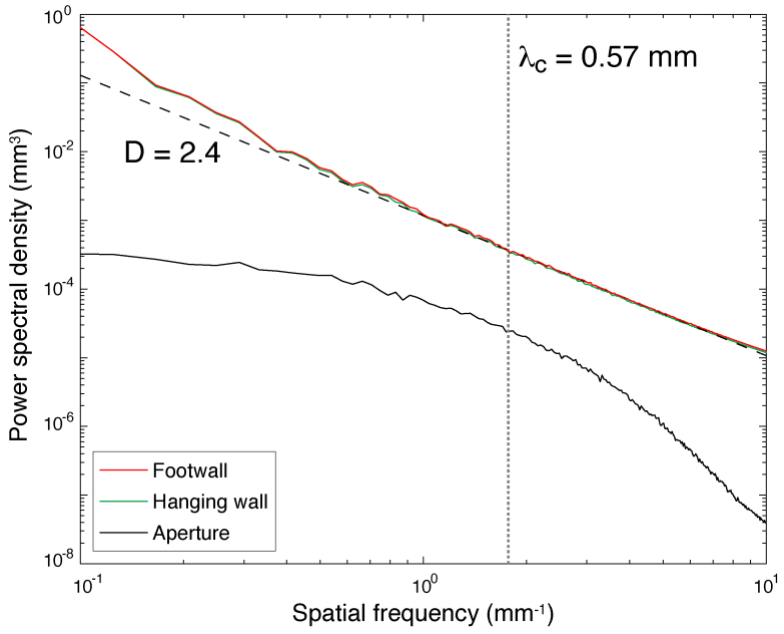

Figure A1 Power spectral density of the footwall, hanging wall, and initial aperture against the spatial frequency (or wavenumber). D and λ_c denote the fractal dimension and the mismatch wavelength that divide mated and unmated spectral regions, respectively.

Table A1 Summary of the fractal characteristics of fracture surfaces in various rock types. L, σ, D, and λ_c represent the fracture length scale, surface roughness, fractal dimension, and mismatch length scale, respectively.

Rock type*	L (mm)	σ (mm)	D	λ_c (mm)	Reference
Andesite (N)	24	0.49	2.4	0.57	This study
Granite (I)	48	1.3	2.5	0.53	Sawayama et al. (2020)
Granite (I)	48	1.7	2.4	0.57	Sawayama et al. (2020)
Granite (I)	20	1.3	2.3	0.7	Ishibashi et al. (2015)
Granite (I)	20	1.966	2.297	0.568	Matsuki et al. (2006)
Granite (I)	95.9	2.02	2.21	4.5	Ogilvie et al. (2006)
Syenite (I)	96.8	1.96	2.18	2.5	Ogilvie et al. (2006)
Gabbro (I)	100	1.945	2.24	2.3	Ogilvie et al. (2006)
Sandstone (I)	100	3.03	2.28	8	Ogilvie et al. (2006)
Granodiorite (I)	97	3.21	2.20	3	Ogilvie et al. (2006)
Tuff (I)	40.96	1.2985	2.305	0.25	Glover et al. (1987; 1998a)
Tuff (N)	13	0.0978	2.41	0.183	Brown (1995)
Tuff (N)	13	0.0682	2.45	0.506	Brown (1995)
Granodiorite (N)	13	0.111	2.32	0.131	Brown (1995)
Sandstone (N)	13	0.156	2.52	0.894	Brown (1995)
metasediment (N)	13	0.085	2.36	0.653	Brown (1995)
Rhyolitic dike (N)	13	0.0985	2.34	0.274	Brown (1995)
Rhyolitic dike (N)	13	0.204	2.4	0.2666	Brown (1995)
Rhyolitic dike (N)	13	0.0864	2.36	0.18	Brown (1995)
Rhyolitic dike (N)	13	0.0668	2.34	1.81	Brown (1995)
Rhyolitic dike (N)	13	0.0894	2.35	0.381	Brown (1995)
Tuff (N)	26	0.189	2.25	0.293	Brown (1995)
Tuff (N)	26	0.147	2.23	0.466	Brown (1995)
Siltstone (N)	13	0.0454	2.48	0.769	Brown (1995)
Chalk (N)	26	0.104	2.41	0.175	Olsson and Brown (1993)
Granite (I)	13	0.201	2.51	1.3	Chen and Spetzler (1993)
Granite (I)	13	0.188	2.49	0.693	Chen and Spetzler (1993)
Granite (I)	13	0.204	2.21	0.714	Chen and Spetzler (1993)
Granodiorite (N)	13	0.222	2.09	0.18	Brown et al. (1986)
Tuff (N)	52	0.758	2.3	3.3	Spengler and Chornak (1984)
Tuff (N)	52	0.702	2.17	0.97	Spengler and Chornak (1984)
Tuff (N)	52	0.962	2.27	0.748	Spengler and Chornak (1984)
Sandstone (I)	42	N/A	N/A	0.45	Glover et al. (1998b)
Granite (I)	42	N/A	N/A	1.40	Glover et al. (1998b)
Granite (I)	42	N/A	N/A	1.10	Glover et al. (1998b)
Diabase (N)	N/A	N/A	2.20	N/A	Brown and Scholz (1985)
Diabase (N)	N/A	N/A	2.19	N/A	Brown and Scholz (1985)
Siltstone (N)	N/A	N/A	2.20	N/A	Brown and Scholz (1985)
Siltstone (N)	N/A	N/A	2.23	N/A	Brown and Scholz (1985)
Siltstone (N)	N/A	N/A	2.20	N/A	Brown and Scholz (1985)
Siltstone (N)	N/A	N/A	2.41	N/A	Bahat and Engelder (1984)
Siltstone (N)	N/A	N/A	2.52	N/A	Bahat and Engelder (1984)

*Fracture types are denoted in the brackets: N: natural joint; I: induced fracture.

Appendix B. Resolution tests

The voxel size potentially affects the absolute value of permeability and formation factor because these quantities are sensitive to the connectivity of the local aperture (Sawayama et al., 2020). To verify this possible effect of voxel size, we analyzed these properties of models with different voxel sizes, preparing 24 mm × 24 mm fracture models using cubic systems with 0.05 mm, 0.1 mm, and 0.2 mm voxels. Figure B1 plots the permeability and formation factor against the mean aperture from the models of each voxel size. At apertures greater than 0.07 mm, both permeability and resistivity in the models with 0.05 mm and 0.1 mm voxels are in good agreement. Although voxel size affects estimates of permeability and formation factor to some degree at apertures smaller than 0.07 mm, the maximum difference in permeability between results with 0.05 mm and 0.1 mm voxels is less than half an order of magnitude (Fig. B1a), and the difference in formation factor is much smaller (Fig. B1b). Because the computational cost is prohibitive at the largest fracture size (144 mm × 144 mm) in a 0.1 mm cubic system, we conclude that the 0.1 mm voxel size is suitable for our discussions of scale dependencies of permeability and formation factor.

Figure B2(a) plots hydraulic tortuosity against mean aperture from the models of each voxel size. The results from the models with 0.05 mm and 0.1 mm voxels show good agreement for mean apertures greater than 0.09 mm. The tortuosity of the smallest voxel size continuously increases with aperture decrease until around a mean aperture of 0.06 mm, which represents a percolation threshold (Fig. 12). Consequently, permeability predicted from the tortuosity and simulated permeability match closely above this threshold (Fig. B2b).

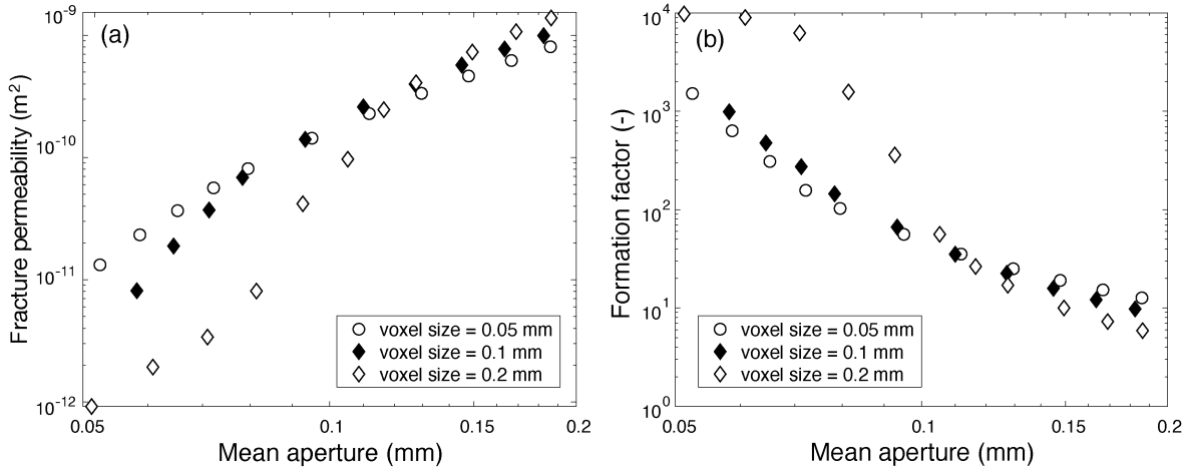

Figure B1 Graphs showing (a) fracture permeability and (b) formation factor with different sizes of voxel as a function of mean aperture. Open diamonds, solid diamonds, and open circles represent the results from 0.2, 0.1, and 0.05 mm voxel sizes, respectively.

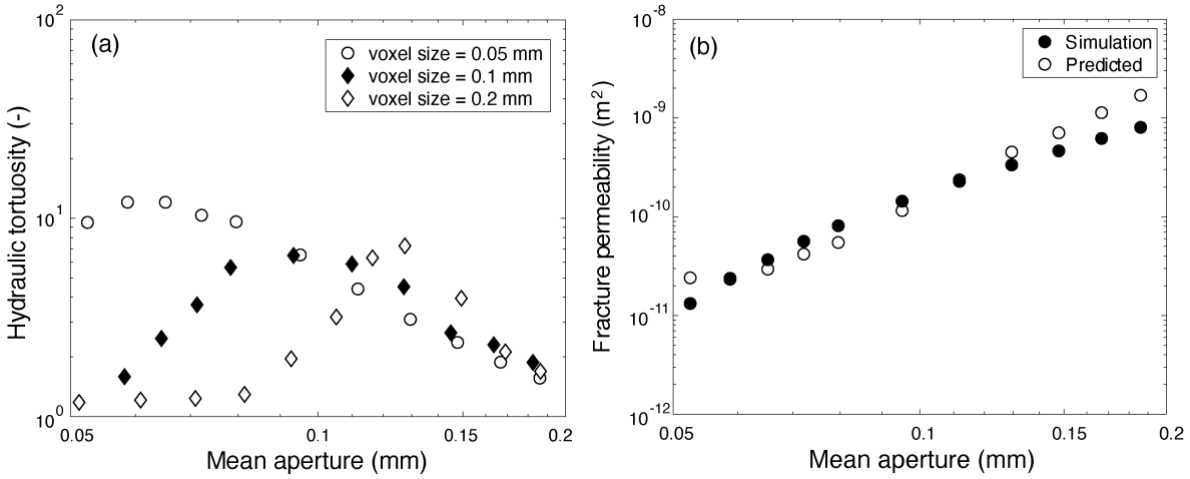

Figure B2 Graphs showing (a) hydraulic tortuosity with different sizes of voxel and (b) simulated and predicted permeability as a function of mean aperture. Open diamonds, solid diamonds, and open circles in Fig. B2(a) represent the results from 0.2, 0.1, and 0.05 mm voxel sizes, respectively. Open and solid circles in Fig. B2(b) denote simulated and predicted results, respectively.

Appendix C. Supplementary data

Supplementary material of all the simulation results can be found, in the online version.

Appendix D. Verification of stochastic fluctuations with 100 different random seeds

Our study used five different random seeds to create fracture models. Although the effect of random seeds is small (Fig. 8), we ran further simulations to better estimate the possible error of the stochastic process. We created and ran simulations in additional fracture models 24 mm in length by using 100 different random seeds with 16 different values of aperture closure in each (1600 models in total). Figure D1, plotting permeability and formation factor against the mean aperture from these models, shows that their fluctuations are negligible at mean apertures greater than 0.1 mm, whereas they show some scatter at smaller mean apertures. Figure D2 shows the relative error of these properties, calculated from the standard deviation of each property at the same mean apertures. Although the error at mean apertures smaller than 0.1 mm is greater than those at larger mean apertures, all results have relative errors smaller than 16%. These fluctuations produce a little scatter in the relationships between permeability and formation factor at smaller apertures, i.e., in less connected regions (Fig. D3); however, note that the empirical parameters α and β in Eq. (12) are not significantly affected by these stochastic fluctuations.

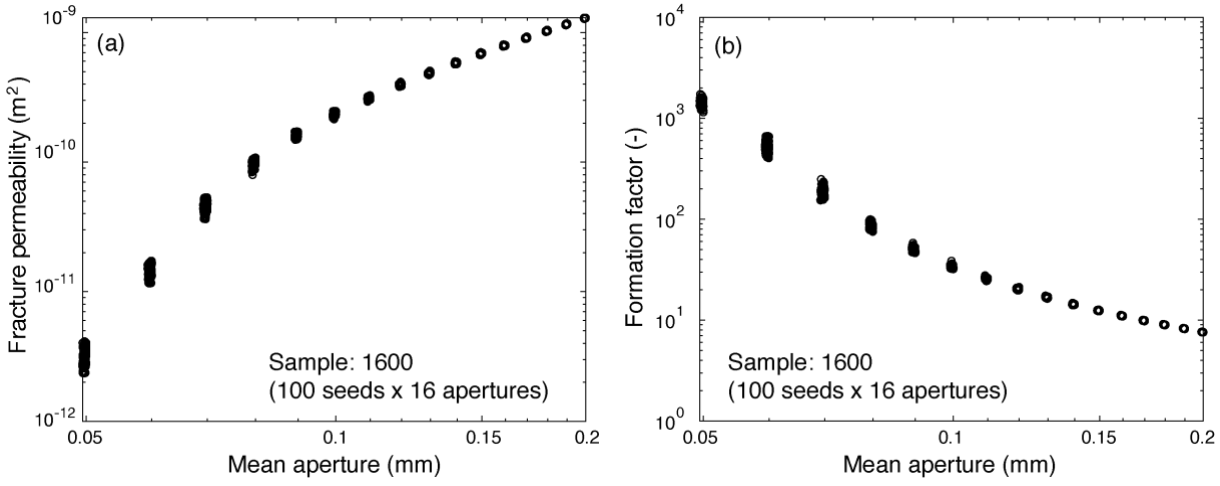

Figure D1 Graphs showing (a) fracture permeability and (b) formation factor of the models with different random seeds as a function of mean aperture.

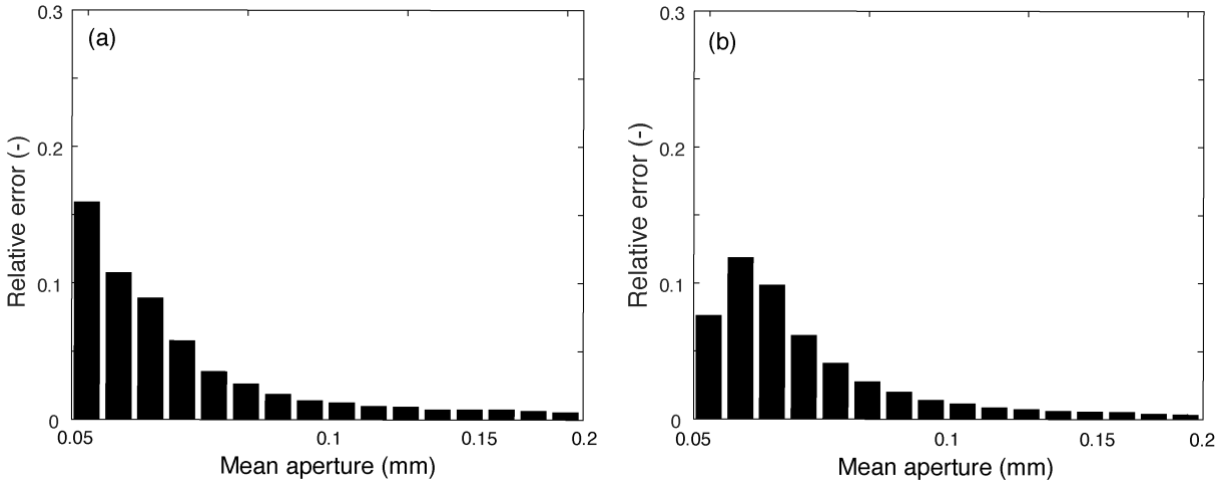

Figure D2 Relative errors of (a) fracture permeability and (b) formation factor with respect to the stochastic process in each mean aperture.

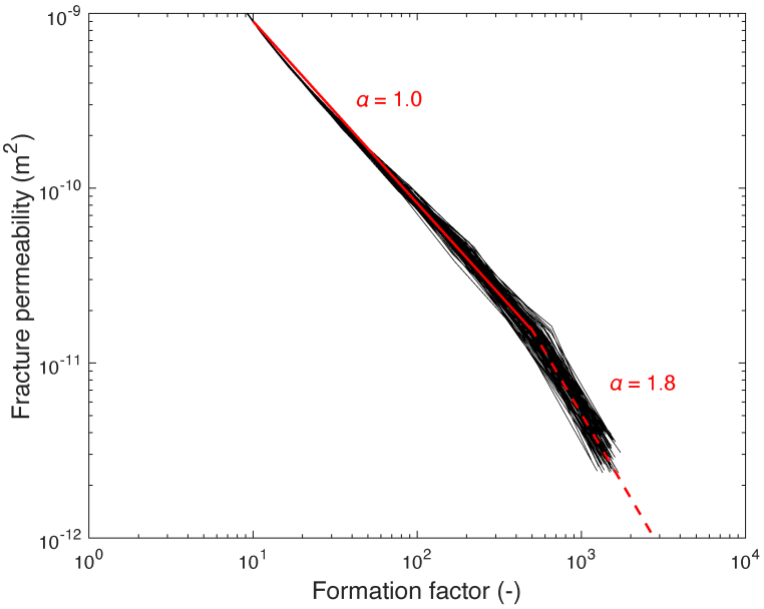

Figure D3 Graphs of fracture permeability versus formation factor from the models with 100 different random seeds. Each solid line represents the results of different random seeds. Red lines denote the prediction lines based on Eq. (12) in which α = 1.0 and β = 8.0 for the solid line and α = 1.8 and β = 5.7 for the dashed line.

Appendix E. Local distribution of electric aperture

We observed the offset between the formation factor predicted from the aperture and the simulated formation factor (Fig. 9b), which may arise from the discrepancy between the local aperture and actual electrical flow paths. To verify this discrepancy, we visualized the distributions of local apertures and electric apertures at a mean aperture of 0.11 mm. The electric aperture is calculated from the local electric current based on Eq. (1). The simulated electric aperture is much greater than the aperture where electrical flow paths are highly connected (Fig. E1a and b). This locally larger electric aperture raises the mean value of the electric aperture above the mean aperture.

One possible concern is that the local aperture in a finite grid cell does not adequately represent the aperture in the case where the aperture significantly changes across a grid cell. In an attempt to reduce this effect, we also calculated the effective electric aperture from a weighted harmonic mean of the local aperture over the cell (Kirkby et al., 2016). The effective electric aperture $d_{e,WE}$ between two adjacent cells is calculated by

$$\frac{1}{d_{e,WE}} = \frac{1}{s_{WC} d_{e,WC}} + \frac{1}{s_{CE} d_{e,CE}}, \tag{E.1}$$

where effective apertures of two adjacent cells ($d_{e,W}$ and $d_{e,E}$) are obtained from the apertures at the midpoint of each cell $d_{e,W}$ or $d_{e,E}$, and the aperture at the common end of the two cells $d_{e,C}$

$$d_{e,WC} = \frac{d_{e,C} - d_{e,W}}{\ln(d_{e,C}) - \ln(d_{e,W})} \tag{E.2a}$$

$$d_{e,CE} = \frac{d_{e,C} - d_{e,E}}{\ln(d_{e,C}) - \ln(d_{e,E})} \tag{E.2b}$$

The weighting factor s is defined by

$$s_{WC} = \frac{\eta_z}{|\boldsymbol{r}_C - \boldsymbol{r}_W|} \tag{E.3a}$$

$$s_{CE} = \frac{\eta_z}{|\boldsymbol{r}_C - \boldsymbol{r}_E|} \tag{E.3b}$$

where η_z is the z component of the unit normal vector to the midpoint between the two surfaces and $\boldsymbol{r}$ is the position vector (Brush and Thomson, 2003). Figure E1c shows the distribution of the calculated effective electric apertures. Although the effective electric apertures are slightly greater than the local

apertures, our simulated electric apertures are greater still. The difference between the mean aperture and electric aperture thus is a characteristic reflecting the local connectivity of electrical flow paths, which cannot be characterized from the aperture alone.

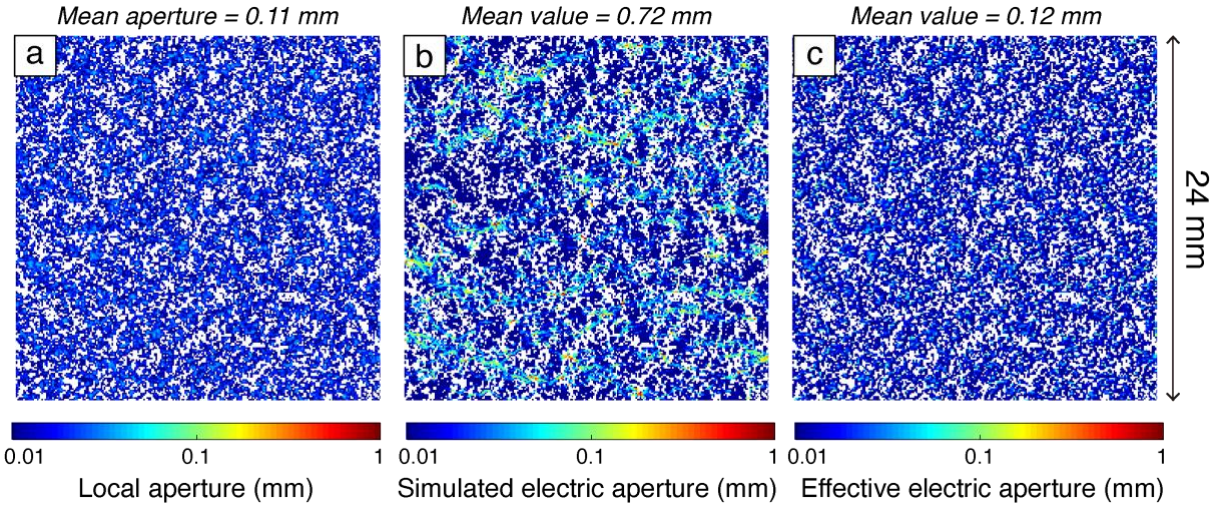

Figure E1 Local distribution of (a) aperture, (b) simulated electric aperture, and (c) effective electric aperture of the model that have 0.11 mm of mean aperture.

Appendix F. Derivation of Equation (14)

The equation (15) represents that changes in the *k–F* relationship with aperture closure can only be characterized by the coefficient α. Based on Eqs. (11) and (12), permeability is the function of the aperture, tortuosity, and porosity, whereas the formation factor is the function of the tortuosity and porosity. Taking them into account, the equation (15) can be rewritten as:

$$\alpha = -\log\frac{k}{k_o}\cdot\left(\log\frac{F}{F_o}\right)^{-1} = -\log\frac{d^2\varphi/\tau^2}{{d_o}^2\varphi_o/{\tau_o}^2}\cdot\left(\log\frac{\tau^2/\varphi}{{\tau_o}^2/\varphi_o}\right)^{-1}, \quad \text{(C.1)}$$

where the subscript zero indicates an arbitrary reference value. Considering the bulk properties including the fracture and matrix with a negligibly small porosity, the fracture porosity φ can be given by the ratio of the aperture d and the model thickness n_z, as $\varphi = d/n_z$. Then substitution of φ into Eq. (C.1) yields:

$$\alpha = -(3\log\frac{d}{d_o} - \log\frac{\tau^2}{\tau^2{}_o}) \cdot (\log\frac{\tau^2}{\tau^2{}_o} - \log\frac{d}{d_o})^{-1} \quad \text{(C.2)}$$

$$\log\frac{\tau^2}{\tau^2{}_o} = \frac{3-\alpha}{1-\alpha}\log\frac{d}{d_o} \quad \text{(C.3)}$$

where the slope $(3-\alpha)/(1-\alpha)$ represents the slope ε in the log-log relationship between tortuosity and aperture (Fig. 8), $\varepsilon = (3-\alpha)/(1-\alpha)$. This is the same form in the Walsh and Brace (1984). In contrast, for the case of fracture permeability where only the fracture aperture is involved, the porosity φ can be assumed to be one, thereby the equation (C.3) should be rewritten as the following form.

$$\log\frac{\tau^2}{\tau^2{}_o} = \frac{2-\alpha}{1-\alpha}\log\frac{d}{d_o} \quad \text{(C.4)}$$

Because the slope $(2-\alpha)/(1-\alpha)$ is equal to the slope ε, the coefficient α is given as: $\alpha = (2-\varepsilon)/(1-\varepsilon)$, which is the specific form for the relationship between fracture permeability and formation factor.